micromachines

MDPI

Article

Analytical Model of the Linearity of a Cryogenic Bipolar Analog Multiplier

Matteo Biscolli [1] and Mattia Borgarino [1,2,*]

[1] Enzo Ferrari Engineering Department, University of Modena and Reggio Emilia, 41125 Modena, Italy; 284250@studenti.unimore.it
[2] Consorzio Nazionale Interuniversitario per le Telecomunicazioni (CNIT), 43124 Parma, Italy
* Correspondence: mattia.borgarino@unimore.it; Tel.: +39-059-2056168

Abstract

This paper studies the nonlinear behavior of a Gilbert cell multiplier. The investigation has been carried out by means of mathematical modeling and Cadence circuit simulations at room and cryogenic temperatures. The circuit has been implemented in the 130 nm SiGe BiCMOS SG13G2 technology by Innovations for High Performance (IHP) Microelectronics (Frankfurt am Oder, Germany). In addition, a similar investigation has been carried out for a Jones modulator. The comparison demonstrated that the Gilbert cell multiplier exhibits better spectral purity, especially at cryogenic temperatures. This suggests the Gilbert multiplier as a promising mixer for quantum computing control circuits, where spectral purity is critical for the quantum gate fidelity.

Keywords: mixer; non-linear modeling; cryogenic; BiCMOS; SFDR

1. Introduction

Mixers are three-port devices ubiquitous in radiofrequency architectures, where they are in charge of frequency translation. This function is usually based on the time variance of a core constituted by transistors driven by a signal large enough for they behave like switches. Transistors used as signal amplifiers may join this core with the aim of adding conversion gain [1]. In this case, we are talking about active mixers, the Gilbert cell being the most popular circuit solution, also for cryogenic applications [2–5]. Otherwise, we are rather talking about passive mixers [6,7]; they provide frequency translation but without gain. The essential function of the switching core is to multiply the incoming input signal by a square wave to be frequency translated. In this way, all spectral components of the input signal are multiplied by all harmonic frequencies nf_{SW} of the square wave. By supposing, for the sake of clarity, that the input signal is a sinusoidal signal, its single frequency f_{INPUT} is translated to the frequencies $f_{INPUT} \pm nf_{SW}$, where n is a positive integer, in force of the well-known trigonometric identity $2cos(\alpha + \beta) = cos(\alpha - \beta) + cos(\alpha + \beta)$. These mixers are classified as multiplier-based, with the aim of distinguishing them from mixers based on non-linear transfer characteristics [8]. For instance, a square-law transfer characteristic processing a sinusoidal tone of frequency f_{INPUT} generates a DC shift and a $2f_{INPUT}$ spectral component, because of the trigonometric identity $2cos^2\alpha = 1 + cos2\alpha$.

In the multiplier-based mixers, the output frequency of usual interest, $f_{INPUT} + f_{SW}$ for up-conversion and $f_{INPUT} - f_{SW}$ for down-conversion, originates from the intermodulation with the square wave fundamental harmonic f_{SW}. Also because of invoking some filtering, it is frequent practice to neglect the other higher-order intermodulation products. In

Check for updates

Academic Editor: Piero Malcovati

Received: 30 September 2026
Revised: 16 October 2026
Accepted: 24 October 2026
Published: 31 October 2026

Copyright: © 2026 by the authors. Licensee MDPI, Basel, Switzerland. This article is an open access article distributed under the terms and conditions of the Creative Commons Attribution (CC BY) license.

this way, you obtain the picture of a mixer as a device multiplying two sinusoidal tones, that is, the incoming sinusoidal signal and the fundamental of the square wave. It is an approximation whose advisability depends on the application. For instance, in a Quantum Processing Unit (QPU) mixers are essential in the radiofrequency architecture of the qubit controller. Since a QPU is essentially an array of qubits, each with its own resonance frequency, unwanted although weak components may jeopardize the quantum fidelity of a quantum gate [9,10]. In the design of the circuitry for a QPU, all spectral components generated during the frequency conversion process should be evaluated.

Conversely, the Gilbert multiplier is a device actually able to operate as a multiplier of two sinusoidal signals [11]. The circuit is bipolar, and it exploits the exponential current-voltage relationship of the forward-biased junction transistor. Over the years, CMOS multipliers were also designed by leveraging the exponential current–voltage relationship of the subthreshold-region-biased MOSFET [12]. Moreover, Gilbert-like arrangements of small-signal transconductors made of saturation-region-biased short-channel MOSFETs were proven as alternative solutions for implementing signal multipliers [13]. Since, because of the first trigonometric identity mentioned above, the product of two sinusoidal signals of frequency f_1 and f_2 generates two spectral components at frequencies $f_1 + f_2$ and $f_1 - f_2$, analog multipliers have been considered as potential mixers [14,15], offering the advantage of generating just the frequencies of interest without the unwanted spectral contributions affecting the multiplier-based mixer, as discussed above. This consideration points out clearly that a Gilbert cell mixer and a Gilbert multiplier are two different circuits operating on two different principles. In the Gilbert cell mixer, some transistors are used as switches, while this is not the case for the Gilbert multiplier. The Gilbert cell mixer needs a large square wave; the Gilbert multiplier does not. In order to avoid confusion, the Gilbert cell mixer should be dubbed more precisely a Jones demodulator [16]. In 1963, Howard Jones conceived this demodulator, that is now, in practice, referred to as the Gilbert cell mixer [17].

Since multiplication is a non-linear algebraic operation, analog multipliers must embed non-linearities. It is expected, thus, that an analog multiplier generates just a couple of frequencies at first order only. Some specific applications, such as the electronics for the QPU cited above, may need a more in-depth study of the spectral purity of which the multiplier is capable. A higher-order analysis is thus required, but few papers address this subject with the necessary sharpness [18–22]. The mathematical analysis is not very sharp, and the comparison with the experimental results is limited in [18]. Atti tried to improve this analysis, but the final results still remain unsatisfactory, and the comparison with measurements or simulations is missing [19]. Kuntman proposes an equivalent circuit model for the non-linear behavior of an analog multiplier, but any mathematical analysis is absent [20]. In spite of being a patent, the reference [21] reports some interesting mathematical results, as it will be pointed out later in this paper, but full analysis and discussion are lacking.

The aim of this paper is to investigate the linearity of a bipolar Gilbert multiplier by means of an analytical model. It is worth pointing out that optimization algorithms demonstrated to be useful and powerful mathematical tools for investigating parameters of relevance in several physical domains [23–26] with a high degree of reliability. Nevertheless, the goal of this paper is to propose an analytical model that may offer mathematical equations that can be used as a guideline in the design process. Of course, in a following step after the fabrication of prototypes, optimization algorithms can also be applied for supplementary purposes.

After an analytical modeling of the generic schematic, the circuit has been implemented in the 130 nm SiGe BiCMOS technology by the Innovations High Performance (IHP)

Microelectronics foundry. The correctness of the analytical model has, therefore, been tested by comparison with circuit simulations. Since the Design Kit (DK) offers cryogenic models for transistors and passive devices, the investigation has been carried out both at the Cryogenic Temperature (CT) of 4 K and at the Room Temperature (RT) of 300 K. In this way, it has also been possible to compare the behavior of the circuit at CT and RT. The availability of a cryogenic DK is of relevance, because it makes it possible to address the linearity of the bipolar Gilbert multiplier in the perspective of its application to the design of cryogenic controllers for qubits.

About the use of bipolar transistors at cryogenic temperature it is worth pointing out that in the last decade the largest amount of quantum computing oriented cryogenic microelectronics is CMOS designed, see for instance [27–41], while some attention has risen up for the use of SiGe Heterojunction Bipolar Transistors (HBT's) available in BiCMOS technologies [4,42–56]. The largest use of cryogenic CMOS may be ascribed partially to the particular physics exhibited by the bipolar transistor operating at 4 K or lower temperatures: the dominant charge transport is no longer drift-diffusion but rather trap-assisted tunneling based [57,58].

Eventually, since the Gilbert cell mixer is widely employed in the cryogenic circuits for quantum computing, for the sake of completeness, this paper also investigates a BiCMOS Jones demodulator with the same approach used for the Gilbert multiplier: analytical modeling of the generic schematic followed by implementation in the 130 nm SiGe BiCMOS SG13G2 technology and by CT and RT circuit simulations. In this way, the paper also compares the spectra generated by the Jones demodulator and the Gilbert multiplier even under cryogenic conditions.

The paper is organized as follows. Section 2 addresses the analytical non-linear modeling of a basic differential transconductor, which is a fundamental sub-circuit of the Gilbert multiplier and of the Gilbert cell mixer, as well. The model is validated by comparison with CT and RT circuit simulations of the differential stage implemented in the IHP technology. Section 3 applies the previous modeling to the Gilbert multiplier to obtain its non-linear model, which is then validated by comparison with CT and RT simulations of its circuit implementation in the IHP technology. This section also proposes some evaluation in terms of Spurious-Free Dynamic Range (SFDR), which is the power ratio between the desired amplitude and the largest unwanted spur in the output spectrum within the specified bandwidth [59–61]. It is a relevant specification for the control signals for qubits. The Jones demodulator undergoes the same investigation in Section 4. Eventually, Section 5 closes the paper by summarizing the main obtained results and by drawing some conclusions.

2. Basic Differential Transconductor

This section focuses on the basic differential transconductor, whose generic schematic Figure 1 depicts on the left. Its core is a symmetric resistive emitter-degenerated bipolar transistor pair biased by the tail current I_0. In particular, Sub-section 2.1 develops the static non-linear model of the DC differential Current-Voltage Transfer Characteristic (CVTC). In Sub-section 2.2, the obtained model is then applied to calculate the spectral components of the differential output currents in the case the differential input voltage signal is a sinusoidal tone. In this way, it is understood implicitly that the circuit is memoryless; otherwise, the more involved Volterra series would be mandatory [62]. Sub-section 2.3 validates the obtained model by comparing the theoretical expectations with the circuit simulations of the IHP technology-implemented circuit depicted on the right in Figure 1.

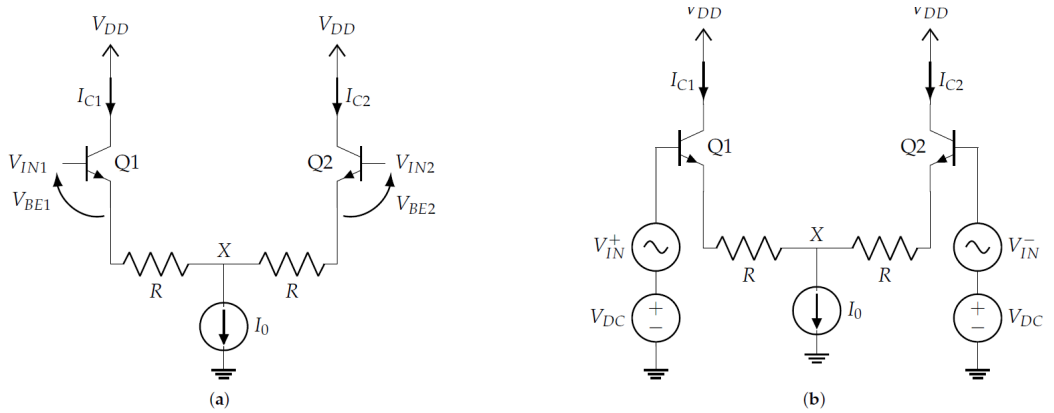


Figure 1. Differential amplifier stage, general schematic (**a**) and circuit implementation (**b**).

2.1. DC Differential Current-Voltage Transfer Characteristic

In Figure 1a DC voltages V_{IN1} and V_{IN2} bias the two identical transistors $Q1$ and $Q2$ in the forward active region, so that you have $\frac{RI_0}{2} + V_X < V_{IN1} < V_{DD}$. The goal of the following analysis is to describe the dependence of the DC differential output current $\Delta I_{OUT} \triangleq I_{C2} - I_{C1}$ on the DC differential input voltage $V_{IN} \triangleq V_{IN1} - V_{IN2}$.

Starting point of the analysis is the usual exponential $I_C - V_{BE}$ characteristic of the bipolar junction transistor:

$$I_C = I_{SC}\left(e^{\frac{V_{BE}}{\eta V_{th}}} - 1\right) \cong I_{SC}e^{\frac{V_{BE}}{\eta V_{th}}} \tag{1}$$

where η is the ideality factor, I_{SC} the saturation current, V_{th} the thermal voltage defined as $V_{th} = \frac{K_B T}{q}$ where K_B is the Boltzmann constant ($\cong 1.36 \times 10^{-23}$ J/K), q the elementary electronic charge ($\cong 1.60 \times 10^{-19}$ C), and T is the absolute temperature in Kelvin.

By assuming $I_E = I_C$, V_{BE1} and V_{BE2} voltages can be expressed as follows:

$$V_{BE1} = V_{IN1} - (R \cdot I_{C1} + V_X) \tag{2}$$
$$V_{BE2} = V_{IN2} - (R \cdot I_{C2} + V_X) \tag{3}$$

The substitution of Equations (2) and (3) into Equation (1) yields the following:

$$I_{C1} = I_{sc}e^{\frac{V_{IN1} - (R \cdot I_{C1} + V_X)}{\eta V_{th}}} \tag{4}$$
$$I_{C2} = I_{sc}e^{\frac{V_{IN2} - (R \cdot I_{C2} + V_X)}{\eta V_{th}}} \tag{5}$$

Due to the assumption $I_E = I_C$, we can also observe that $I_0 = I_{C2} + I_{C1}$, and we can normalize each collector current respect to I_0:

$$\frac{I_{C1}}{I_0} = \frac{I_{C1}}{I_{C1} + I_{C2}} = \frac{I_{sc}e^{\frac{V_{IN1} - (RI_{C1} + V_X)}{\eta V_{th}}}}{I_{sc}e^{\frac{V_{IN1} - (RI_{C1} + V_X)}{\eta V_{th}}} + I_{sc}e^{\frac{V_{IN2} - (RI_{C2} + V_X)}{\eta V_{th}}}} \tag{6}$$
$$\frac{I_{C2}}{I_0} = \frac{I_{C2}}{I_{C1} + I_{C2}} = \frac{I_{sc}e^{\frac{V_{IN2} - (RI_{C2} + V_X)}{\eta V_{th}}}}{I_{sc}e^{\frac{V_{IN1} - (RI_{C1} + V_X)}{\eta V_{th}}} + I_{sc}e^{\frac{V_{IN2} - (RI_{C2} + V_X)}{\eta V_{th}}}} \tag{7}$$

and by simplifying by I_{SC}:

$$\frac{I_{C1}}{I_0} = \frac{e^{\frac{V_{IN1}-(RI_{C1}+V_X)}{\eta V_{th}}}}{e^{\frac{V_{IN1}-(RI_{C1}+V_X)}{\eta V_{th}}} + e^{\frac{V_{IN2}-(RI_{C2}+V_X)}{\eta V_{th}}}} \tag{8}$$

$$\frac{I_{C2}}{I_0} = \frac{e^{\frac{V_{IN2}-(RI_{C2}+V_X)}{\eta V_{th}}}}{e^{\frac{V_{IN1}-(RI_{C1}+V_X)}{\eta V_{th}}} + e^{\frac{V_{IN2}-(RI_{C2}+V_X)}{\eta V_{th}}}} \tag{9}$$

The mathematical expression for $\frac{\Delta I_{OUT}}{I_0}$ is thus as follows:

$$\frac{I_{C1}-I_{C2}}{I_0} = \frac{\Delta I_{OUT}}{I_0} = \frac{I_{C1}}{I_0} - \frac{I_{C2}}{I_0} = \frac{e^{\frac{V_{IN1}-(RI_{C1}+V_X)}{\eta V_{th}}} - e^{\frac{V_{IN2}-(RI_{C2}+V_X)}{\eta V_{th}}}}{e^{\frac{V_{IN1}-(RI_{C1}+V_X)}{\eta V_{th}}} + e^{\frac{V_{IN2}-(RI_{C2}+V_X)}{\eta V_{th}}}} \tag{10}$$

By gathering the term $e^{\frac{V_{IN2}-(RI_{C2}+V_X)}{\eta V_{th}}}$, we obtain the following mathematical expression:

$$\frac{\Delta I_{OUT}}{I_0} = \frac{e^{\frac{V_{IN1}-V_{IN2}-(RI_{C1}-RI_{C2})}{\eta V_{th}}} - 1}{e^{\frac{V_{IN1}-V_{IN2}-(RI_{C1}-RI_{C2})}{\eta V_{th}}} + 1} \tag{11}$$

$$= \frac{e^{\frac{\Delta V_{IN}-(R\Delta I_{OUT})}{\eta V_{th}}} - 1}{e^{\frac{\Delta V_{IN}-R\Delta I_{OUT}}{\eta V_{th}}} + 1} = \frac{e^{\frac{\Delta V_{IN}-R\Delta I_{OUT}}{2\eta V_{th}}} - e^{-\frac{\Delta V_{IN}-R\Delta I_{OUT}}{2\eta V_{th}}}}{e^{\frac{\Delta V_{IN}-(R\Delta I_{OUT}}{\eta V_{th}}} + e^{-\frac{\Delta V_{IN}-R\Delta I_{OUT}}{2\eta V_{th}}}} \tag{12}$$

and thus by reminding that $\frac{e^x-e^{-x}}{e^x+e^{-x}} \triangleq \tanh(x)$, we can put Equation (12) in the following form:

$$\Delta I_{OUT} = I_0 \tanh\left(\frac{\Delta V_{IN} - R\Delta I_{OUT}}{2\eta V_{th}}\right) \tag{13}$$

Reminding that the term ΔI_{OUT} is a function of ΔV_{IN} it may be useful rewriting the Equation (13) as follows:

$$\Delta I_{OUT} = I_0 \tanh\left[\frac{\Delta V_{IN} - R\Delta I_{OUT}(\Delta V_{IN})}{2\eta V_{th}}\right] \tag{14}$$

Equation (13) is a transcendental equation in the argument ΔI_{OUT}. It has no closed-form solution, and it can be solved only by numerical iteration. Following the famous Fermi's advice "When in doubt, expand in a power series" [63], we can spend effort to obtain an approximated closed-form solution by applying a Taylor series expansion whose general form is as follows:

$$f(x) \triangleq \sum_{n=0}^{\infty} \frac{f^{(n)}(x_0)}{n!}(x-x_0)^n \tag{15}$$

where the $f^{(n)}(x_0) = \left.\frac{df^{(n)}(x)}{d\Delta V_{IN}}\right|_{x=x_0}$. For the sake of simplicity, we stop the expansion at the third order:

$$\Delta I_{OUT} \approx \Delta I_{OUT}(\Delta V_{IN} = \Delta V_{IN0}) + \left.\frac{d\Delta I_{OUT}}{d\Delta V_{IN}}\right|_{\Delta V_{IN}=\Delta V_{IN0}} (\Delta V_{IN} - \Delta V_{IN0}) \tag{16}$$

$$+ \frac{1}{2}\left.\frac{d^2\Delta I_{OUT}}{d\Delta V_{IN}^2}\right|_{\Delta V_{IN}=\Delta V_{IN0}} (\Delta V_{IN} - \Delta V_{IN0})^2 + \frac{1}{6}\left.\frac{d^3\Delta I_{OUT}}{d\Delta V_{IN}^3}\right|_{\Delta V_{IN}=\Delta V_{IN0}} (\Delta V_{IN} - \Delta V_{IN0})^3$$

In particular, we desire to calculate this series by expanding around the origin, so that we have $\Delta V_{IN0} = 0$:

$$\Delta I_{OUT} \approx \Delta I_{OUT}(\Delta V_{IN} = 0) + \left.\frac{d\Delta I_{OUT}}{d\Delta V_{IN}}\right|_{\Delta V_{IN}=0} \Delta V_{IN} + \frac{1}{2}\left.\frac{d^2\Delta I_{OUT}}{d\Delta V_{IN}^2}\right|_{\Delta V_{IN}=0} \Delta V_{IN}^2 + \frac{1}{6}\left.\frac{d^3\Delta I_{OUT}}{d\Delta V_{IN}^3}\right|_{\Delta V_{IN}=0} \Delta V_{IN}^3 \quad (17)$$

Since $\Delta I_{OUT} = 0$ for $\Delta V_{IN} = 0$ (balanced distribution of current on the two branches of the circuit in Figure 1), we can conclude immediately that $\Delta I_{OUT}(\Delta V_{IN} = 0) = 0$. Further calculations, detailed in Appendix A, yields the other three terms:

$$\left.\frac{d\Delta I_{OUT}}{d\Delta V_{IN}}\right|_{\Delta V_{IN}=0} = \frac{\frac{I_0}{2\eta V_{th}}}{1 + \frac{I_0 R}{2\eta V_{th}}} \quad (18)$$

$$\left.\frac{d^2\Delta I_{OUT}}{d\Delta V_{IN}^2}\right|_{\Delta V_{IN}=0} = 0 \quad (19)$$

$$\left.\frac{d^3\Delta I_{OUT}}{d\Delta V_{IN}^3}\right|_{\Delta V_{IN}=0} = -\frac{I_0}{4(\eta V_{th})^3} \frac{1}{\left(1 + \frac{I_0 R}{2\eta V_{th}}\right)^4} \quad (20)$$

Substituting Equations (18)–(20) into Equation (17), we obtain the closed form solution of Equation (14) in an approximation:

$$\Delta I_{OUT} = \frac{\frac{I_0}{2\eta V_{th}}}{1 + \frac{RI_0}{2\eta V_{th}}} \Delta V_{IN}(t) - \frac{I_0}{24(\eta V_{th})^3} \frac{1}{\left(1 + \frac{I_0 R}{2\eta V_{th}}\right)^4} [\Delta V_{IN}(t)]^3 \quad (21)$$

2.2. Harmonic Analysis

Equation (21) can be used to assess the spectrum of ΔI_{OUT} when $\Delta V_{IN}(t) = \Delta V_{IN} \cos(\omega t)$, being ΔV_{IN} the amplitude and ω the angular frequency. From Equation (21) we obtain the following:

$$\Delta I_{OUT} = \frac{\frac{I_0}{2\eta V_{th}}}{1 + \frac{RI_0}{2\eta V_{th}}} \Delta V_{IN} \cos(\omega t) - \frac{I_0}{24(\eta V_{th})^3} \frac{1}{\left(1 + \frac{I_0 R}{2\eta V_{th}}\right)^4} [\Delta V_{IN} \cos(\omega t)]^3 \quad (22)$$

By applying the trigonometric identity $4\cos^3(x) = cos(3x) + 3cos(x)$ we get:

$$\Delta I_{OUT} = \frac{\frac{I_0}{2\eta V_{th}}}{1+\frac{RI_0}{2\eta V_{th}}}\Delta V_{IN}\cos(\omega t) - \frac{I_0}{24(\eta V_{th})^3}\frac{1}{\left(1+\frac{I_0 R}{2\eta V_{th}}\right)^4}\Delta V_{IN}^3\frac{\cos(3\omega t)+3\cos(\omega t)}{4} = \tag{23}$$

$$= \frac{\frac{I_0}{2\eta V_{th}}}{1+\frac{RI_0}{2\eta V_{th}}}\Delta V_{IN}\cos(\omega t) - 3\frac{I_0}{24(\eta V_{th})^3}\frac{1}{\left(1+\frac{I_0 R}{2\eta V_{th}}\right)^4}\Delta V_{IN}^3\frac{\cos(\omega t)}{4}$$

$$- \frac{I_0}{24(\eta V_{th})^3}\frac{1}{\left(1+\frac{I_0 R}{2\eta V_{th}}\right)^4}\Delta V_{IN}^3\frac{\cos(3\omega t)}{4}$$

Gathering the contributions according to the harmonics provides the amplitudes a_1 and a_3 of the fundamental and third harmonics, respectively:

$$a_1 = \frac{\frac{I_0}{2\eta V_{th}}}{1+\frac{RI_0}{2V_{th}}}\Delta V_{IN} - \frac{3I_0}{96(\eta V_{th})^3}\frac{1}{\left(1+\frac{I_0 R}{2\eta V_{th}}\right)^4}\Delta V_{IN}^3 \tag{24}$$

$$a_3 = -\frac{I_0}{96(\eta V_{th})^3}\frac{1}{\left(1+\frac{I_0 R}{2\eta V_{th}}\right)^4}\Delta V_{IN}^3 \tag{25}$$

As expected, the third-order non-linear coefficient a_3 is negative, and it reduces a_1. By substituting Equations (24) and (25) into the previous mathematical expression of ΔI_{OUT} you obtain the following:

$$\Delta I_{OUT} = a_1\cos(\omega t) + a_3\cos(3\omega t) \tag{26}$$

It is worth calculating the following ratio:

$$\left|\frac{a_1}{a_3}\right| = \left|\frac{\frac{I_0\Delta V_{IN}}{2\eta V_{th}+RI_0}+3a_3}{a_3}\right| = \left|3+\frac{1}{a_3}\frac{I_0\Delta V_{IN}}{2\eta V_{th}+RI_0}\right| \tag{27}$$

From the definition of *SFDR* provided in the Introduction, the substitution of Equation (25) into Equation (27) yields the following:

$$SFDR = 20\log_{10}\left|\frac{a_1}{a_3}\right| = 20\log_{10}\left|-6\frac{(2\eta V_{th}+RI_0)^3}{\eta V_{th}\Delta V_{IN}^2}+3\right| \tag{28}$$

The *SFDR* is, therefore, a positive number if $x > -2$ or $x < -4$, where x is defined as follows:

$$x = -6\frac{(2\eta V_{th}+RI_0)^3}{\eta V_{th}\Delta V_{IN}^2} \tag{29}$$

Equation (29) defines two possible intervals of values of ΔV_{IN} for which $SFDR > 0$: $\Delta V_{IN} > \xi$ and $0<\Delta V_{IN} < \xi/\sqrt{2}$, being the following:

$$\xi = \sqrt{\frac{3(2\eta V_{th}+RI_0)^3}{\eta V_{th}}} \tag{30}$$

Outside these two intervals, you have $|a_1|$ lower than $|a_3|$.

2.3. Validation

The generic schematic of the differential transconductor, on the left in Figure 1, has been implemented in the circuit on the right in Figure 1 using the IHP SG13G2 technology. For the Cadence circuit simulations carried out at RT (CT), I_0 was kept equal to 117 µA (243 µA). These values are in order to maximize the current gain β of the HBT.

Conversely, the bias voltage V_{DD} was kept equal to 1.2 V and the resistance R to 800 Ω, regardless of the temperature. The value of R was chosen low enough to keep the transistors correctly polarized in the forward active region. From the simulations of the Gummel plots, the ideality factor η results in 1.08 (26.37) at RT (CT). The value of η at CT is the signature of the dominant trap-assisted tunneling charge transport [57,58]. Table 1 summarizes the values used for the simulations together with the thermal voltage V_{th}.

Table 1. Adopted values for the simulations of the differential transconductor in Figure 1.

Temperature [K]	I_0 [A]	R [Ω]	η	V_{th} [mV]	V_{DD} [V]
300	117×10^{-6}	800	1.08	26	1.2
4	243×10^{-6}	800	26.37	0.347	1.2

Figure 2 compares the DC differential CVTC calculated from Equation (21) with the simulated one for ΔV_{IN} spanning from −0.6 V to 0.6 V. The figure shows good agreement in the interval from about −0.2 V to about 0.2 V both at RT and CT.

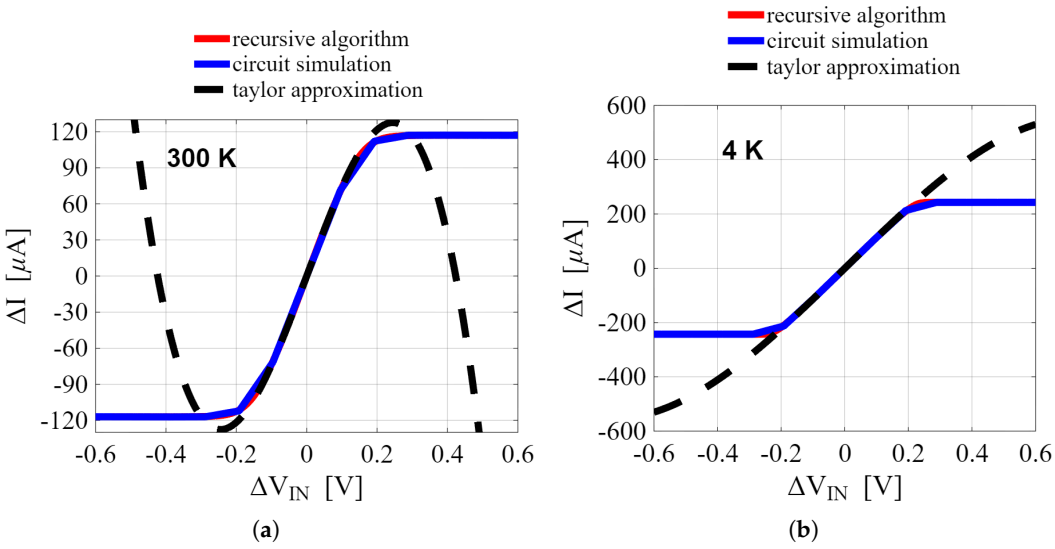


Figure 2. DC differential CVTC for 300 K (**a**) and 4 K (**b**).

Moreover, the CVTC was also obtained by a recursive numerical solution of Equation (13) carried out with MATLAB (version 2025A). The figure shows that the numerically obtained CVTC is also in good agreement with the previous two at both temperatures. Defined the differential input knee voltage $\Delta V_{IN,knee}$ as the intersection between the tangent of the CVTC for $\Delta V_{IN,knee} = 0$ and the saturation currents $\pm I_0$, Equation (18) yields $\Delta V_{IN,knee} = 2\eta V_{th} + RI_0$, as detailed in Appendix B. By replacing the values in Table 1, you obtain $\Delta V_{IN,knee}$ = 149.4 mV (212.6 mV) at RT (CT), in good agreement with the extrapolation you can obtain from Figure 2.

When $\Delta V_{IN}(t) = \Delta V_{IN} \cos(\omega t)$, the amplitude ΔV_{IN} was kept equal to 100 mV, large enough to allow the steering of the tail current between the two branches at both RT and

CT. The frequency was chosen equal to 1 GHz. This frequency is very useful because it is common to several qubit platforms (superconducting, semiconductor, trapped ion) [64]. Table 2 reports the values of the fundamental and third-order harmonics obtained from the analytical model via Equations (24) and (25).

Table 2. Harmonic amplitudes according to the analytical model.

Temperature	300 K		4 K	
Harmonics	1st tone (a_1) [A]	3rd tone (a_3) [A]	1st tone (a_1) [A]	3rd tone (a_3) [A]
Results	7.490×10^{-5}	1.090×10^{-6}	1.137×10^{-4}	1.811×10^{-7}

Even in the present case, the model expectations have been compared with MATLAB and circuit simulations. About MATLAB simulations, the input voltage signal ΔV_{IN} is sampled at n discrete time instants $t_k = k\Delta t$, producing a sequence of samples ΔV_{IN_k}, with $k = 0, 1, \ldots, n-1$. For each sample, the corresponding output current ΔI_{OUT1_k} is determined by iteratively solving Equation (13). In this way, a set of couples (t_k,ΔI_{OUT1_k}) is obtained from which the MATLAB DFT (Discrete Fourier Transform) function computes the spectrum. Figure 3 shows the obtained results.

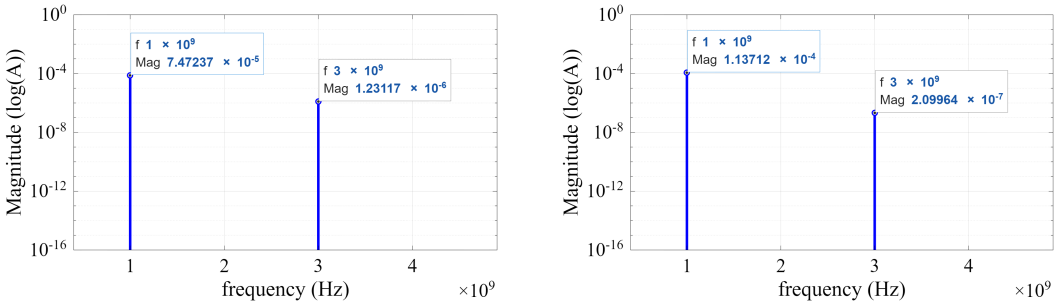


Figure 3. MATLAB DFT output for 300 K (**a**) and 4 K (**b**).

As far as the circuit simulation, transient simulations were carried out on the circuit implemented in the SG13G2 technology. Figure 4 shows the computed spectra.

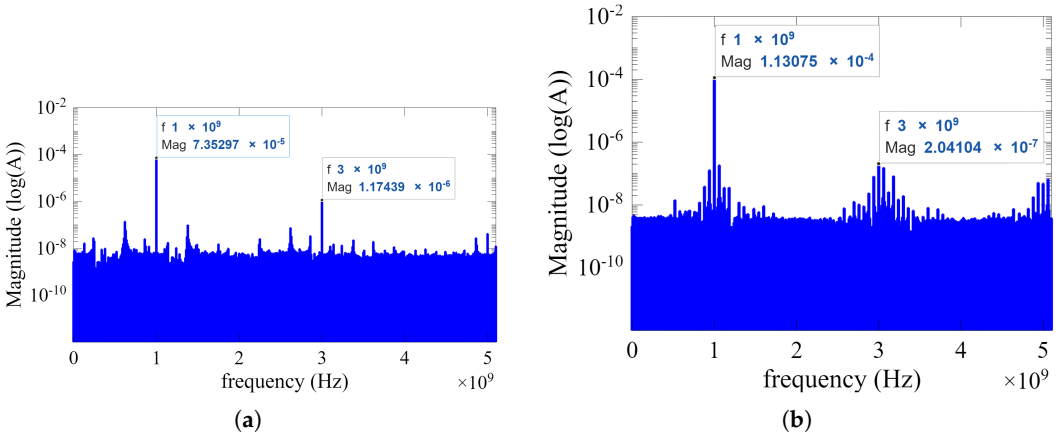


Figure 4. Spectra for 300K (**a**) and 4K (**b**) from circuit simulation.

Table 3 provides an overall comparison of the fundamental and third-order harmonics obtained from the analytical model, MATLAB numerical solution and circuit simulations.

Table 3. Overall comparison between circuit simulations, MATLAB solutions, and analytical model.

Parameters		Circuit Simulation	MATLAB Solution		Analytical Model	
T **[K]**	**Tone**	**Value [A]**	**Value [A]**	**Error [%]**	**Value [A]**	**Error [%]**
300	1st	7.353×10^{-5}	7.4724×10^{-5}	−1.6	7.490×10^{-5}	−1.8
	3rd	1.1744×10^{-6}	1.2312×10^{-6}	−4.8	1.089×10^{-6}	7.3
4	1st	1.1307×10^{-4}	1.1351×10^{-4}	−0.39	1.137×10^{-4}	−0.56
	3rd	2.0411×10^{-7}	2.1241×10^{-7}	−4.1	1.811×10^{-7}	11.3

The result is very satisfying, because the relative error is lower than 10%. It is thus possible to close this section by concluding that both numerical solutions and circuit simulations validate, both at RT and CT, the non-linear analytical model of the differential transconductor depicted in Figure 1.

3. Gilbert Multiplier

Figure 5 shows that the Gilbert multiplier is composed of two subcircuits: an input differential amplifier and a Gilbert cell. The figure also shows that four differential pairs, as investigated in Section 2, are present. In particular, the differential pair formed by the transistors Q3 and Q4 (Q5 and Q6) is a differential pair without resistive degeneration, and it exploits the collector current I_{C1} (I_{C2}) of Q1 (Q2) as tail current.

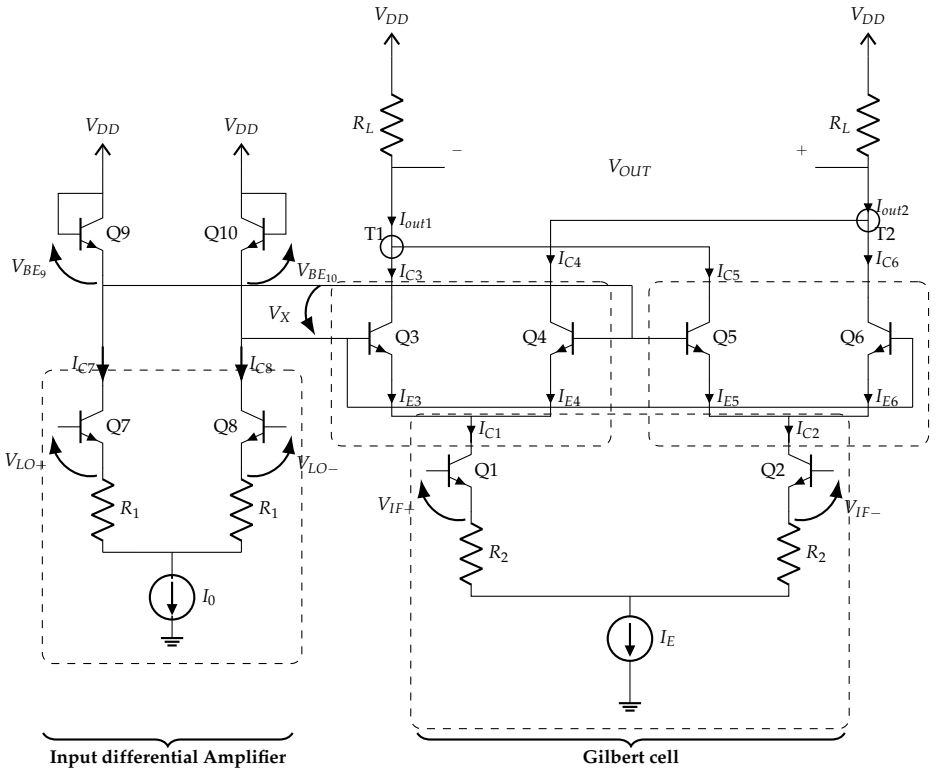


Figure 5. Generic schematic of the Gilbert multiplier.

According to Sub-section 2.1, collector and emitter currents can be assumed identical ($I_{C_i} = I_{E_i},\ i = 1, \ldots 10$) and the following equations can be written down:

$$\Delta I_{78} = I_0 \tanh\left(\frac{\Delta V_{LO} - R_1 \Delta I_{78}}{2\eta V_{th}}\right) \tag{31}$$

$$\Delta I_{12} = I_E \tanh\left(\frac{\Delta V_{IF} - R_2 \Delta I_{12}}{2\eta V_{th}}\right) \tag{32}$$

with $\Delta I_{78} \triangleq I_{C7} - I_{C8}$, $\Delta I_{12} \triangleq I_{C1} - I_{C2}$, $\Delta V_{LO} \triangleq V_{LO+} - V_{LO-}$, and $\Delta V_{IF} \triangleq V_{IF+} - V_{IF-}$. The differential pair Q7-Q8 is loaded by the transistors Q9-Q10 in a diode configuration. The output voltage V_X is thus

$$\begin{aligned} V_X &= (V_{DD} - V_{BE_{10}}) - (V_{DD} - V_{BE_9}) = V_{BE_9} - V_{BE_{10}} \\ &= \eta V_{th} \ln\left(\frac{I_{C7}}{I_{sc}}\right) - V_{th} \ln\left(\frac{I_{C8}}{I_{sc}}\right) = \eta V_{th} \ln\left(\frac{I_{C7}}{I_{C8}}\right) \end{aligned} \tag{33}$$

From the definition of ΔI_{78} and the relation $I_0 = I_{C7} + I_{C8}$ we can rewrite I_{C7} and I_{C8} as follows:

$$I_{C7} = \frac{I_0 + \Delta I_{78}}{2} \tag{34}$$

$$I_{C8} = \frac{I_0 - \Delta I_{78}}{2} \tag{35}$$

By substituting Equations (34) and (35) into Equation (33) we can write the following:

$$V_X = \eta V_{th} \ln\left(\frac{\frac{I_0 + \Delta I_{78}}{2}}{\frac{I_0 - \Delta I_{78}}{2}}\right) = \eta V_{th} \ln\left(\frac{1 + \frac{\Delta I_{78}}{I_0}}{1 - \frac{\Delta I_{78}}{I_0}}\right) \tag{36}$$

By reminding that $2\text{atanh}(x) = \ln\left(\frac{1+x}{1-x}\right)$, the previous equation can be reformulated as follows:

$$V_X = 2\eta V_{th} \frac{1}{2} \ln\left(\frac{1 + \frac{\Delta I_{78}}{I_0}}{1 - \frac{\Delta I_{78}}{I_0}}\right) = 2\eta V_{th}\, \text{atanh}\left(\frac{\Delta I_{78}}{I_0}\right) \tag{37}$$

in agreement with [21].

The differential output voltage V_{OUT} can be calculated as follows:

$$V_{OUT} = V_{CC} - I_{out2} R_L - (V_{CC} - I_{out1} R_L) = R_L (I_{out1} - I_{out2}) \tag{38}$$

Current balance at node $T1$ and $T2$ yields $I_{out1} = I_{C3} + I_{C5}$ and $I_{out2} = I_{C4} + I_{C6}$, respectively, so that you can write the following:

$$V_{OUT} = R_L [I_{C3} + I_{C5} - (I_{C4} + I_{C6})] = R_L [(I_{C3} - I_{C4}) + (I_{C5} - I_{C6})] \tag{39}$$

Equation (13) can be applied to the Q3–Q4 and Q5–Q6 transistor pairs but with $R = 0$ to obtain the following:

$$I_{C3} - I_{C4} = I_{C1} \tanh\left(\frac{V_X}{2\eta V_{th}}\right) \tag{40}$$

$$I_{C5} - I_{C6} = I_{C2} \tanh\left(-\frac{V_X}{2\eta V_{th}}\right) = -I_{C2} \tanh\left(\frac{V_X}{2\eta V_{th}}\right) \tag{41}$$

By substituting Equations (40) and (41) into Equation (39) the output voltage results to be the following:

$$V_{OUT} = R_L\left[I_{C1}\tanh\left(\frac{V_X}{2\eta V_{th}}\right) - I_{C2}\tanh\left(\frac{V_X}{2\eta V_{th}}\right)\right] = \\ = R_L\tanh\left(\frac{V_X}{2\eta V_{th}}\right)(I_{C1} - I_{C2}) = R_L\tanh\left(\frac{V_X}{2\eta V_{th}}\right)\Delta I_{12} \tag{42}$$

Because of Equation (37), Equation (42) yields the following:

$$V_{OUT} = R_L\Delta I_{12}\tanh\left[\frac{2\eta V_{th}\,\mathrm{atanh}\left(\frac{\Delta I_{78}}{I_0}\right)}{2\eta V_{th}}\right] \\ = R_L\Delta I_{12}\frac{\Delta I_{78}}{I_0} \tag{43}$$

It is worth reminding that, according to the results obtained in Section 2, ΔI_{12} and ΔI_{78} are recursively defined functions in the two variables ΔV_{LO} and ΔV_{RF}, respectively. Because of Equation (43) V_{OUT} results thus recursevely defined in ΔV_{LO} and ΔV_{RF}, as well. With $x \triangleq V_{RF}$ and $y \triangleq V_{LO}$ from Equation (13) you can write the following:

$$g(x) = I_E\tanh\left[\frac{x - R_2 g(x)}{2\eta V_{th}}\right] \tag{44}$$

and

$$h(y) = I_0\tanh\left[\frac{x - R_1 h(y)}{2\eta V_{th}}\right] \tag{45}$$

and thus Equation (43) becomes:

$$V_{OUT} = \frac{R_L}{I_0}g(x)h(y) = \frac{R_L}{I_0}f(x,y) \tag{46}$$

$$\tag{47}$$

with $f(x,y) \triangleq g(x)h(y)$.

By extension of the approach used in Sub-section 2.1, we provide an approximated closed form of $f(x,y)$ by means of a bidimensional Taylor series:

$$f(x,y) = f(x_0,y_0) + \sum_{n=1}^{\infty}\left\{\sum_{k=0}^{n}\frac{1}{k!(n-k)!}\frac{\delta^n f}{\delta^{n-k}x\delta^k y}\bigg|_{x_0,y_0}(x-x_0)^{n-k}(y-y_0)^k\right\} \tag{48}$$

Since we are interested in approximating V_{OUT} around $\Delta V_{IF} = 0$ and $\Delta V_{LO} = 0$, for which $\Delta I_{12} = 0$ and $\Delta I_{78} = 0$, you have $x_0 = 0$, $y_0 = 0$, and $f(x_0,y_0) = 0$. Thus, you can write the following:

$$f(x,y) = \sum_{n=1}^{\infty}\left\{\sum_{k=0}^{n}\frac{1}{k!(n-k)!}\frac{\delta^n f}{\delta^{n-k}x\delta^k y}\bigg|_{0,0}(x)^{n-k}(y)^k\right\} \tag{49}$$

By defining $Q_n = \frac{R_L}{I_0}\sum_{k=0}^{n}\frac{1}{k!(n-k)!}\frac{\delta^n f}{\delta^{n-k}x\delta^k y}\Big|_{0,0}x^{n-k}y^k$ from Equation (46) we obtain $V_{OUT} = \sum_{i=1}^{4}Q_i$ with the following:

$$Q_1 = \frac{R_L}{I_0}\left[\frac{\delta f}{\delta x}\bigg|_{(0,0)} x + \frac{\delta f}{\delta y}\bigg|_{(0,0)} y\right] \tag{50}$$

$$Q_2 = \frac{R_L}{I_0}\left[\frac{1}{2}\frac{\delta^2 f}{\delta^2 x}\bigg|_{(0,0)} x^2 + \frac{\delta^2 f}{\delta x \delta y}\bigg|_{(0,0)} xy + \frac{1}{2}\frac{\delta^2 f}{\delta^2 y}\bigg|_{(0,0)} y^2\right] \tag{51}$$

$$Q_3 = \frac{R_L}{I_0}\left[\frac{1}{6}\frac{\delta^3 f}{\delta x^3}\bigg|_{(0,0)} x^3 + \frac{1}{2}\frac{\delta^3 f}{\delta x^2 \delta y}\bigg|_{(0,0)} x^2 y + \frac{1}{2}\frac{\delta^3 f}{\delta x \delta y^2}\bigg|_{(0,0)} xy^2 + \frac{1}{6}\frac{\delta^3 f}{\delta y^3}\bigg|_{(0,0)} y^3\right] \tag{52}$$

$$Q_4 = \frac{R_L}{I_0}\left[\frac{1}{24}\frac{\delta^4 f}{\delta x^4}\bigg|_{(0,0)} x^4 + \frac{1}{6}\frac{\delta^4 f}{\delta x^3 \delta y}\bigg|_{(0,0)} x^3 y + \frac{1}{4}\frac{\delta^4 f}{\delta x^2 \delta y^2}\bigg|_{(0,0)} x^2 y^2 + \frac{1}{6}\frac{\delta^4 f}{\delta x \delta y^3}\bigg|_{(0,0)} xy^3 + \frac{1}{24}\frac{\delta^4 f}{\delta y^4}\bigg|_{(0,0)} y^4\right] \tag{53}$$

Because of the definition of $f(x, y)$, the mathematical expressions above can be further calculated as follows:

$$Q_1 = \frac{R_L}{I_0}\left[\frac{\delta g(x)}{\delta x}\bigg|_{x=0} h(0)x + g(0)\frac{\delta h(y)}{\delta y}\bigg|_{y=0} y\right] \tag{54}$$

$$Q_2 = \frac{R_L}{I_0}\left[\frac{1}{2}\frac{\delta^2 g(x)}{\delta x^2}\bigg|_{x=0} h(0)x^2 + \frac{\delta g(x)}{\delta x}\bigg|_{x=0}\frac{\delta h(y)}{\delta y}\bigg|_{y=0} xy + \frac{1}{2}\frac{\delta^2 h(y)}{\delta y^2}\bigg|_{y=0} g(0)y^2\right] \tag{55}$$

$$\begin{aligned} Q_3 = \frac{R_L}{I_0}\Bigg[&\frac{1}{6}\frac{\delta^3 g(x)}{\delta x^3}\bigg|_{x=0} h(0)x^3 + \frac{1}{2}\frac{\delta^2 g(x)}{\delta x^2}\bigg|_{x=0}\frac{\delta h(y)}{\delta y}\bigg|_{y=0} x^2 y \\ &+\frac{1}{2}\frac{\delta g(x)}{\delta x}\bigg|_{x=0}\frac{\delta^2 h(y)}{\delta y^2}\bigg|_{y=0} xy^2 + \frac{1}{6}\frac{\delta^3 h(y)}{\delta y^3}\bigg|_{y=0} g(0)y^3\Bigg] \end{aligned} \tag{56}$$

$$\begin{aligned} Q_4 = \frac{R_L}{I_0}\Bigg[&\frac{1}{24}\frac{\delta^4 g(x)}{\delta x^4}\bigg|_{x=0} h(0)x^4 + \frac{1}{6}\frac{\delta^3 g(x)}{\delta x^3}\bigg|_{x=0}\frac{\delta h(y)}{\delta y}\bigg|_{y=0} x^3 y \\ &+\frac{1}{4}\frac{\delta^2 g(x)}{\delta x^2}\bigg|_{x=0}\frac{\delta^2 h(y)}{\delta y^2}\bigg|_{y=0} x^2 y^2 + \frac{1}{6}\frac{\delta g(x)}{\delta x}\bigg|_{x=0}\frac{\delta^3 h(y)}{\delta y^3}\bigg|_{y=0} xy^3 + \frac{1}{24}\frac{\delta^4 h(y)}{\delta y^4}\bigg|_{y=0} g(0)y^4\Bigg] \end{aligned} \tag{57}$$

Now, the derivatives of Equations $g(x)$ and $h(y)$ correspond to the derivatives obtained in Appendix A. So, taking each derivative and evaluating it at the origin, we can observe that $g(0) = h(0) = 0$. We can also notice that the second derivatives of both functions, $\frac{\delta^2 g(x)}{\delta x^2}$ and $\frac{\delta^2 h(y)}{\delta y^2}$, are equal to zero, because the functions are symmetric around the origin. In this way, we obtain:

$$Q_1 = 0 \tag{58}$$

$$Q_2 = \frac{R_L}{I_0}\frac{\delta g(x)}{\delta x}\bigg|_{x=0}\frac{\delta h(y)}{\delta y}\bigg|_{y=0} xy \tag{59}$$

$$Q_3 = 0 \tag{60}$$

$$Q_4 = \frac{R_L}{I_0}\left[\frac{1}{6}\frac{\delta^3 g(x)}{\delta x^3}\bigg|_{x=0}\frac{\delta h(y)}{\delta y}\bigg|_{y=0} x^3 y + \frac{1}{6}\frac{\delta g(x)}{\delta x}\bigg|_{x=0}\frac{\delta^3 h(y)}{\delta y^3}\bigg|_{y=0} xy^3\right] \tag{61}$$

Eventually, the substitution of Equations (18) and (20) into Equations (59) and (61) yields the following:

$$Q_2 = \frac{R_L}{I_0}\frac{\frac{I_0}{2\eta V_{th}}}{1+\frac{R_1 I_0}{2\eta V_{th}}}\frac{\frac{I_E}{2\eta V_{th}}}{1+\frac{R_2 I_E}{2\eta V_{th}}} xy \tag{62}$$

$$Q_4 = -\frac{R_L}{I_0}\left[\frac{1}{6}\frac{\frac{I_0}{4(\eta V_{th})^3}}{(1+\frac{R_1 I_0}{2\eta V_{th}})^4}\frac{\frac{I_E}{2\eta V_{th}}}{1+\frac{R_2 I_E}{2\eta V_{th}}} xy^3 + \frac{1}{6}\frac{\frac{I_E}{4(\eta V_{th})^3}}{(1+\frac{R_2 I_E}{2\eta V_{th}})^4}\frac{\frac{I_0}{2\eta V_{th}}}{1+\frac{R_1 I_0}{2\eta V_{th}}} x^3 y\right] \tag{63}$$

Bringing terms to common denominator and applying algebraic simplifications yields the final mathematical expressions:

$$Q_2 = \frac{R_L}{I_0}\frac{I_0}{2\eta V_{th}+R_1 I_0}\frac{I_E}{2\eta V_{th}+R_2 I_E}xy \tag{64}$$

$$Q_4 = -\frac{R_L}{I_0}\left[\frac{1}{6}\frac{4\eta V_{th} I_0}{(2\eta V_{th}+R_1 I_0)^4}\frac{I_E}{2\eta V_{th}+R_2 I_E}xy^3 + \frac{1}{6}\frac{4\eta V_{th} I_E}{(2\eta V_{th}+R_2 I_E)^4}\frac{I_0}{2\eta V_{th}+R_1 I_0}x^3 y\right] \tag{65}$$

Assuming x and y sinusoidal voltages:

$$x = V_{IF}\cos(\omega_{IF}t) \tag{66}$$

$$y = V_{LO}\cos(\omega_{LO}t) \tag{67}$$

the term Q_2 becomes the following:

$$Q_2 = \frac{R_L}{I_0}\frac{I_0}{2\eta V_{th}+R_1 I_0}\frac{I_E}{2\eta V_{th}+R_2 I_E}V_{IF}V_{LO}\cos(\omega_{IF}t)\cos(\omega_{LO}t) \tag{68}$$

Reminding the trigonometric identity $2cos(\alpha)cos(\beta) = cos(\alpha-\beta)+cos(\alpha+\beta)$ Equation (68) takes the following form:

$$Q_2 = \frac{R_L}{I_0}\frac{I_0}{2\eta V_{th}+R_1 I_0}\frac{I_E}{2\eta V_{th}+R_2 I_E}V_{IF}V_{LO}\frac{\cos[(\omega_{IF}+\omega_{LO})t]+\cos[(\omega_{IF}-\omega_{LO})t]}{2} \tag{69}$$

This results in second-order intermodulation products.

The term Q_4 generates second- and fourth-order intermodulation products. By substituting Equations (66) and (67) into Equation (65), we obtain the following:

$$\begin{aligned} Q_4 = &-\frac{R_L}{6I_0}\frac{4\eta V_{th} I_0}{(2\eta V_{th}+R_1 I_0)^4}\frac{I_E}{2\eta V_{th}+R_2 I_E}V_{IF}\cos(\omega_{IF}t)[V_{LO}\cos(\omega_{LO}t)]^3 + \\ &-\frac{R_L}{6I_0}\frac{4\eta V_{th} I_E}{(2\eta V_{th}+R_2 I_E)^4}\frac{I_0}{2\eta V_{th}+R_1 I_0}[V_{IF}\cos(\omega_{IF}t)]^3 V_{LO}\cos(\omega_{LO}t) \end{aligned} \tag{70}$$

Now, by reminding the trigonometric identity $4cos^3(\alpha) = cos(3\alpha)+3cos(\alpha)$ Equation (70) results in the following:

$$\begin{aligned} Q_4 = &-\frac{R_L}{6I_0}\frac{4\eta V_{th} I_0}{(2\eta V_{th}+R_1 I_0)^4}\frac{I_E}{2\eta V_{th}+R_2 I_E}V_{IF}V_{LO}^3\cos(\omega_{IF}t)\frac{\cos(3\omega_{LO}t)+3\cos(\omega_{LO}t)}{4} + \\ &-\frac{R_L}{6I_0}\frac{4\eta V_{th} I_E}{(2\eta V_{th}+R_2 I_E)^4}\frac{I_0}{2\eta V_{th}+R_1 I_0}V_{IF}^3 V_{LO}\cos(\omega_{LO}t)\frac{\cos(3\omega_{IF}t)+3\cos(\omega_{IF}t)}{4} \end{aligned} \tag{71}$$

Applying again the previous trigonometic identities Equation (71) leads to eight distinct tones:

$$\begin{aligned} Q_4 = &-\frac{R_L}{6I_0}\frac{4\eta V_{th} I_0}{(2\eta V_{th}+R_1 I_0)^4}\frac{I_E}{2\eta V_{th}+R_2 I_E}V_{IF}V_{LO}^3\frac{\cos[(3\omega_{LO}+\omega_{IF})t]+\cos[(3\omega_{LO}-\omega_{IF})]}{8} + \\ &-\frac{R_L}{6I_0}\frac{4\eta V_{th} I_0}{(2\eta V_{th}+R_1 I_0)^4}\frac{I_E}{2\eta V_{th}+R_2 I_E}V_{IF}V_{LO}^3\frac{3\cos[(\omega_{LO}+\omega_{IF})t]+3\cos[(\omega_{LO}-\omega_{IF})]}{8} + \\ &-\frac{R_L}{6I_0}\frac{4\eta V_{th} I_E}{(2\eta V_{th}+R_2 I_E)^4}\frac{I_0}{2\eta V_{th}+R_1 I_0}V_{IF}^3 V_{LO}\frac{\cos[(3\omega_{IF}+\omega_{LO})t]+\cos[(3\omega_{IF}-\omega_{LO})t]}{8} + \\ &\frac{R_L}{6I_0}\frac{4\eta V_{th} I_E}{(2\eta V_{th}+R_2 I_E)^4}\frac{I_0}{2\eta V_{th}+R_1 I_0}V_{IF}^3 V_{LO}\frac{3\cos[(\omega_{IF}+\omega_{LO})t]+3\cos[(\omega_{IF}-\omega_{LO})t]}{8} \end{aligned} \tag{72}$$

Denoting as $V_{OUT}(\omega_{LO}\pm\omega_{IF})$ the amplitude of the second-order intermodulation products, as $V_{OUT}(3\omega_{IF}\pm\omega_{LO})$ the amplitudes of the tones at frequency $3\omega_{IF}\pm\omega_{LO}$, and

as $V_{OUT}(\omega_{IF} \pm 3\omega_{LO})$ the amplitudes of the tones at the frequency $\omega_{IF} \pm 3\omega_{LO}$, we can write the following:

$$\begin{aligned} V_{OUT}(\omega_{LO} \pm \omega_{IF}) = & \frac{R_L}{2} \frac{1}{2\eta V_{th} + R_1 I_0} \frac{I_E}{2\eta V_{th} + R_2 I_E} V_{IF} V_{LO} \\ & - \frac{R_L}{4} \frac{\eta V_{th}}{(2\eta V_{th} + R_1 I_0)^4} \frac{I_E}{2\eta V_{th} + R_2 I_E} V_{IF} V_{LO}^3 \\ & - \frac{R_L}{4} \frac{I_E \eta V_{th}}{(2\eta V_{th} + R_2 I_E)^4} \frac{1}{2\eta V_{th} + R_1 I_0} V_{IF}^3 V_{LO} \end{aligned} \quad (73)$$

$$V_{OUT}(3\omega_{LO} \pm \omega_{IF}) = -\frac{R_L}{12} \frac{\eta V_{th}}{(2\eta V_{th} + R_1 I_0)^4} \frac{I_E}{2\eta V_{th} + R_2 I_E} V_{IF} V_{LO}^3 \quad (74)$$

$$V_{OUT}(\omega_{LO} \pm 3\omega_{IF}) = -\frac{R_L}{12} \frac{I_E \eta V_{th}}{(2\eta V_{th} + R_2 I_E)^4} \frac{1}{2\eta V_{th} + R_1 I_0} V_{IF}^3 V_{LO} \quad (75)$$

3.1. Circuit Simulation and Comparison

For sake of validation of Equations (73)–(75), the generic schematic in Figure 5 has been implemented in the circuit depicted in Figure 6 by using the IHP SG13G2 technology. Since in Equations (73)–(75) amplitude exhibits specific dependence on V_{RF} and V_{LO}, we performed transient simulations by sweeping V_{RF} (V_{LO}) while keeping V_{LO} (V_{RF}) constant.

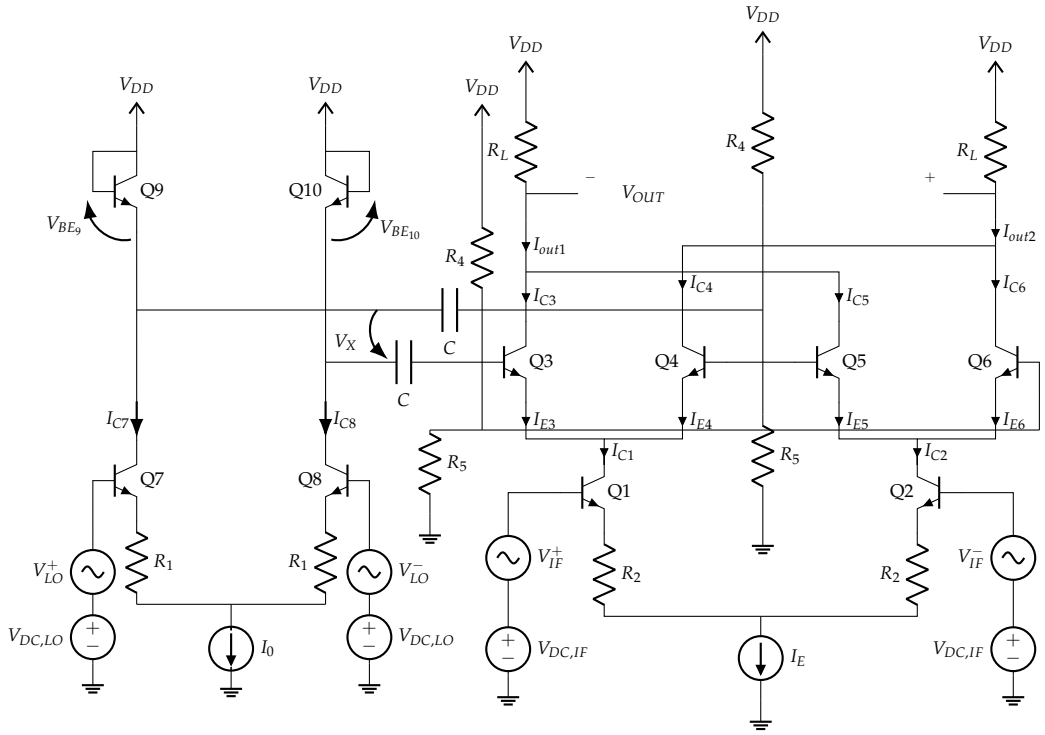


Figure 6. Circuit of Gilbert multiplier implemented in the IHP technology.

Table 4 reports the adopted values for resistors and capacitors, Table 5 for the bias, and Table 6 for transistor sizes at RT and CT.

Table 4. Resistors and capacitors.

Temp. [K]	R_L [Ω]	R_1 [Ω]	R_2 [Ω]	R_4 [kΩ]	R_5 [kΩ]	C [pF]
300	2000	800	800	15	150	100
4	2000	800	800	20	160	100

The value of R_L was chosen at the best trade-off between gain and correct biasing of the transistors $Q_3 - Q_6$. The value of the degeneration resistors R_1 and R_2 was chosen at the best trade-off between linearization and bias point. The values of the resistors R_4 and R_5 were chosen to bias correctly the transistors $Q_3 - Q_6$. The capacitance of the capacitor C was chosen high enough for the capacitor to act as a coupling capacitor.

Table 5. Bias voltages and tail currents.

Temp. [K]	I_0 [µA]	I_E [µA]	V_{DD} [V]	$V_{DC,IF}$ [V]	$V_{DC,LO}$ [V]
300	117	117	2.5	1.2	1.2
4	243	243	2.5	1.2	1.2

The values of the currents I_0 and I_E were chosen to maximize the beta current gain of the HBT. The value of V_{DD} was chosen to be compliant with the voltage headroom required by the biasing of the Gilbert cell. The values of $V_{DC,IF}$ and $V_{DC,LO}$ were chosen for the correct biasing of the differential pairs.

Table 6. Transistor sizes; m1 refers to the number of emitters; the effective emitter area is thus $m1 \times W \times L$.

Temp. [K]	W [nm]	L [nm]	m_1	η
300	70	900	1	1.08
4	70	900	1	26.37

The HBT sizes W and L were chosen to maximize the beta current gain, which is indeed dependent on the collector current density rather than the collector current itself. The values of η were obtained by fitting the Gummel plots.

Transient simulations were carried out by sweeping V_{LO} (V_{IF}) from 1μ V to 100 mV with V_{IF} (V_{LO}) kept constant at 100 mV. In particular, the local oscillator frequency ω_{LO} was kept equal to 1 GHz and the intermediate frequency ω_{IF} equal to 140 MHz. The amplitudes of the output tones calculated from Equations (73)–(75) and reported in Tables 7–10 have been compared with the simulated amplitudes reported in Tables 11–14. Moreover, for the sake of readability, Figures 7–12 report calculated and simulated amplitudes.

Table 7. Calculated tone amplitudes at 300 K for sweeping V_{LO} and V_{IF} = 100 mV.

V_{LO} [mV]	$V_{OUT}(\omega_{LO} \pm \omega_{IF})$ [V]	$V_{OUT}(\omega_{LO} \pm 3\omega_{IF})$ [V]	$V_{OUT}(3\omega_{LO} \pm \omega_{IF})$ [V]
0.001	5.0180×10^{-07}	7.3017×10^{-09}	7.3017×10^{-19}
0.01	5.0180×10^{-06}	7.3017×10^{-08}	7.3017×10^{-16}
0.1	5.0180×10^{-05}	7.3017×10^{-07}	7.3017×10^{-13}
1	5.0180×10^{-04}	7.3017×10^{-06}	7.3017×10^{-10}
10	5.0158×10^{-03}	7.3017×10^{-05}	7.3017×10^{-07}
100	4.7990×10^{-02}	7.3017×10^{-04}	7.3017×10^{-04}
Reference	Figure 7a	Figure 8a	Figure 9a

Table 8. Calculated tone amplitudes at 300 K for sweeping V_{IF} and V_{LO} = 100 mV.

V_{IF} [mV]	$V_{OUT}(\omega_{LO} \pm \omega_{IF})$ [V]	$V_{OUT}(\omega_{LO} \pm 3\omega_{IF})$ [V]	$V_{OUT}(3\omega_{LO} \pm \omega_{IF})$ [V]
0.001	5.0180×10^{-07}	7.3017×10^{-19}	7.3017×10^{-09}
0.01	5.0180×10^{-06}	7.3017×10^{-16}	7.3017×10^{-08}
0.1	5.0180×10^{-05}	7.3017×10^{-13}	7.3017×10^{-07}
1	5.0180×10^{-04}	7.3017×10^{-10}	7.3017×10^{-06}
10	5.0158×10^{-03}	7.3017×10^{-07}	7.3017×10^{-05}
100	4.7990×10^{-02}	7.3017×10^{-04}	7.3017×10^{-04}
Reference	Figure 7b	Figure 8b	Figure 9b

Table 9. Calculated tone amplitudes at 4 K for sweeping V_{LO} and V_{IF} = 100 mV.

V_{LO} [mV]	$V_{OUT}(\omega_{LO} \pm \omega_{IF})$ [V]	$V_{OUT}(\omega_{LO} \pm 3\omega_{IF})$ [V]	$V_{OUT}(3\omega_{LO} \pm \omega_{IF})$ [V]
0.001	5.3519×10^{-07}	8.4800×10^{-10}	8.4800×10^{-20}
0.01	5.3519×10^{-06}	8.4800×10^{-09}	8.4800×10^{-17}
0.1	5.3519×10^{-05}	8.4800×10^{-08}	8.4800×10^{-14}
1	5.3519×10^{-04}	8.4800×10^{-07}	8.4800×10^{-11}
10	5.3516×10^{-03}	8.4800×10^{-06}	8.4800×10^{-08}
100	5.3264×10^{-02}	8.4800×10^{-05}	8.4800×10^{-05}
Reference	Figure 10a	Figure 12a	Figure 11a

Table 10. Calculated tone amplitudes at 4 K for sweeping V_{IF} and V_{LO} = 100 mV.

V_{IF} [mV]	$V_{OUT}(\omega_{LO} \pm \omega_{IF})$ [V]	$V_{OUT}(\omega_{LO} \pm 3\omega_{IF})$ [V]	$V_{OUT}(3\omega_{LO} \pm \omega_{IF})$ [V]
0.001	5.3519×10^{-07}	8.4800×10^{-20}	8.4800×10^{-10}
0.01	5.3519×10^{-06}	8.4800×10^{-17}	8.4800×10^{-09}
0.1	5.3519×10^{-05}	8.4800×10^{-14}	8.4800×10^{-08}
1	5.3519×10^{-04}	8.4800×10^{-11}	8.4800×10^{-07}
10	5.3516×10^{-03}	8.4800×10^{-08}	8.4800×10^{-06}
100	5.3264×10^{-02}	8.4800×10^{-05}	8.4800×10^{-05}
Reference	Figure 10b	Figure 12b	Figure 11b

Table 11. Simulated tone amplitudes at 300 K for sweeping V_{LO} and V_{IF} = 100 mV.

V_{LO} [mV]	$V_{OUT}(\omega_{LO} \pm \omega_{IF})$ [V]	$V_{OUT}(\omega_{LO} \pm 3\omega_{IF})$ [V]	$V_{OUT}(3\omega_{LO} \pm \omega_{IF})$ [V]
0.001	4.6330×10^{-07}	6.9274×10^{-09}	1.2925×10^{-14}
0.01	4.6330×10^{-06}	6.9274×10^{-08}	1.1127×10^{-13}
0.1	4.6330×10^{-05}	6.9274×10^{-07}	1.6486×10^{-12}
1	4.6330×10^{-04}	6.9274×10^{-06}	7.2195×10^{-10}
10	4.6310×10^{-03}	6.9252×10^{-05}	7.1587×10^{-07}
100	4.4132×10^{-02}	6.6560×10^{-04}	8.1567×10^{-04}
Reference	Figure 7a	Figure 8a	Figure 9a

Table 12. Simulated tone amplitudes a 300 K for sweeping V_{IF} and V_{LO} = 100 mV.

V_{IF} [mV]	$V_{OUT}(\omega_{LO} \pm \omega_{IF})$ [V]	$V_{OUT}(\omega_{LO} \pm 3\omega_{IF})$ [V]	$V_{OUT}(3\omega_{LO} \pm \omega_{IF})$ [V]
0.001	4.6060×10^{-07}	1.2783×10^{-13}	8.4457×10^{-09}
0.01	4.6060×10^{-06}	1.2785×10^{-12}	8.4457×10^{-08}
0.1	4.6060×10^{-05}	1.3022×10^{-11}	8.4457×10^{-07}
1	4.6060×10^{-04}	6.4265×10^{-10}	8.4456×10^{-06}
10	4.6042×10^{-03}	5.8303×10^{-07}	8.4431×10^{-05}
100	4.4132×10^{-02}	6.6560×10^{-04}	8.1567×10^{-04}
Reference	Figure 7b	Figure 8b	Figure 9b

Table 13. Simulated tone amplitudes at 4 K for sweeping V_{LO} and V_{IF} = 100 mV.

V_{LO} [mV]	$V_{OUT}(\omega_{LO} \pm \omega_{IF})$ [V]	$V_{OUT}(\omega_{LO} \pm 3\omega_{IF})$ [V]	$V_{OUT}(3\omega_{LO} \pm \omega_{IF})$ [V]
0.001	5.2134×10^{-07}	6.9732×10^{-10}	2.1976×10^{-16}
0.01	5.2134×10^{-06}	6.9732×10^{-09}	2.7170×10^{-15}
0.1	5.2134×10^{-05}	6.9731×10^{-08}	6.2791×10^{-13}
1	5.2134×10^{-04}	6.9657×10^{-07}	6.0625×10^{-10}
10	5.2155×10^{-03}	6.2385×10^{-06}	5.9957×10^{-07}
100	5.3140×10^{-02}	9.3929×10^{-05}	1.6049×10^{-04}
Reference	Figure 10a	Figure 12a	Figure 11a

Table 14. Simulated tone amplitudes at 4 K for sweeping V_{IF} and V_{LO} = 100 mV.

V_{IF} [mV]	$V_{OUT}(\omega_{LO} \pm \omega_{IF})$ [V]	$V_{OUT}(\omega_{LO} \pm 3\omega_{IF})$ [V]	$V_{OUT}(3\omega_{LO} \pm \omega_{IF})$ [V]
0.001	5.3366×10^{-07}	2.9581×10^{-15}	2.0341×10^{-09}
0.01	5.3366×10^{-06}	1.0588×10^{-13}	2.0341×10^{-08}
0.1	5.3366×10^{-05}	3.2405×10^{-12}	2.0341×10^{-07}
1	5.3365×10^{-04}	2.3202×10^{-10}	2.0339×10^{-06}
10	5.3367×10^{-03}	7.1311×10^{-07}	1.9477×10^{-05}
100	5.3140×10^{-02}	9.3929×10^{-05}	1.6049×10^{-04}
Reference	Figure 10b	Figure 12b	Figure 11b

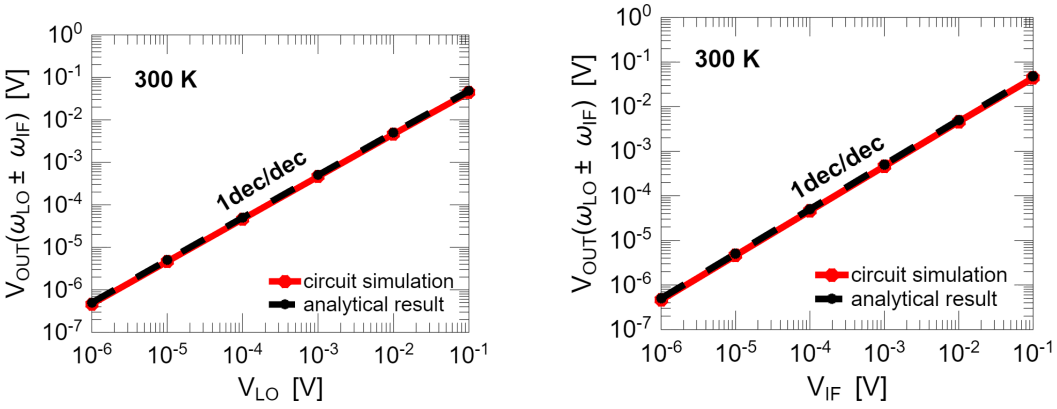


Figure 7. Amplitude of second-order intermodulation products versus V_{LO} (**a**) and V_{IF} (**b**) for $V_{IF} = 100$ mV and $V_{LO} = 100$ mV, respectively, at 300 K.

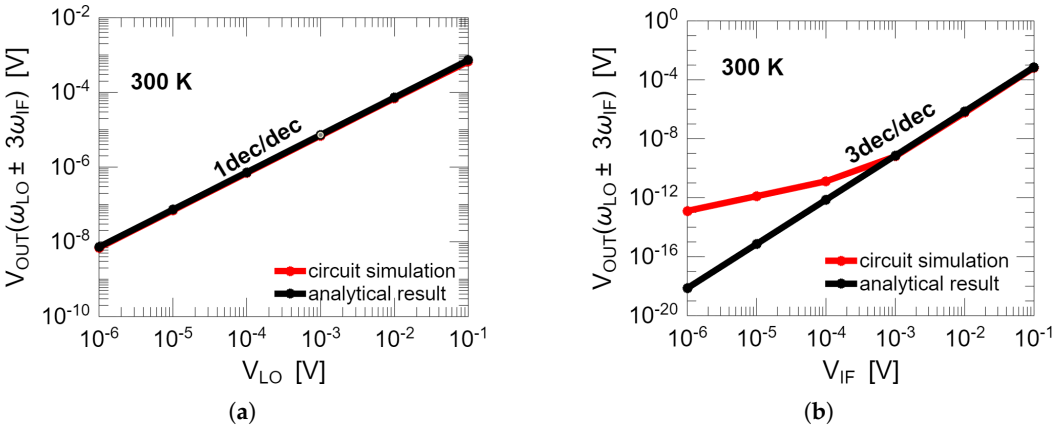


Figure 8. Amplitude of fourth-order intermodulation products at $\omega_{LO} \pm 3\omega_{IF}$ versus V_{LO} (**a**) and V_{IF} (**b**) for $V_{IF} = 100$ mV and $V_{LO} = 100$ mV, respectively, at 300 K.

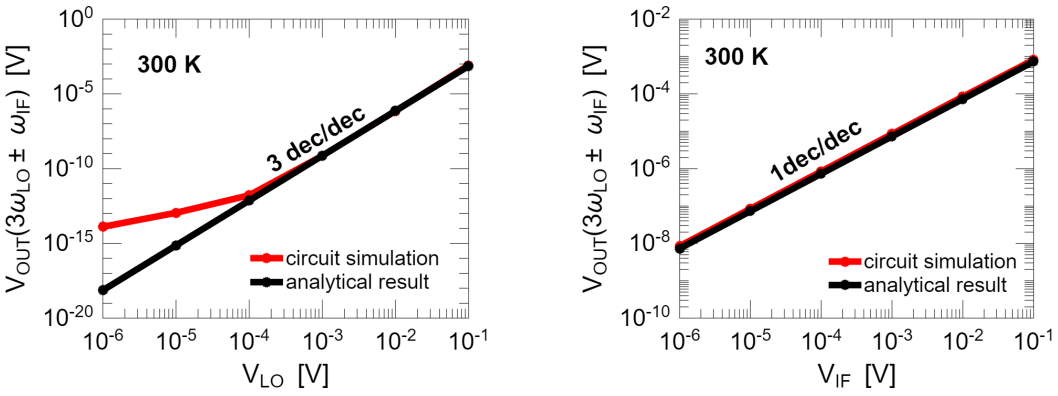


Figure 9. Amplitude of fourth-order intermodulation products at $3\omega_{LO} \pm \omega_{IF}$ versus V_{LO} (**a**) and V_{IF} (**b**) for $V_{IF} = 100$ mV and $V_{LO} = 100$ mV, respectively, at 300 K.

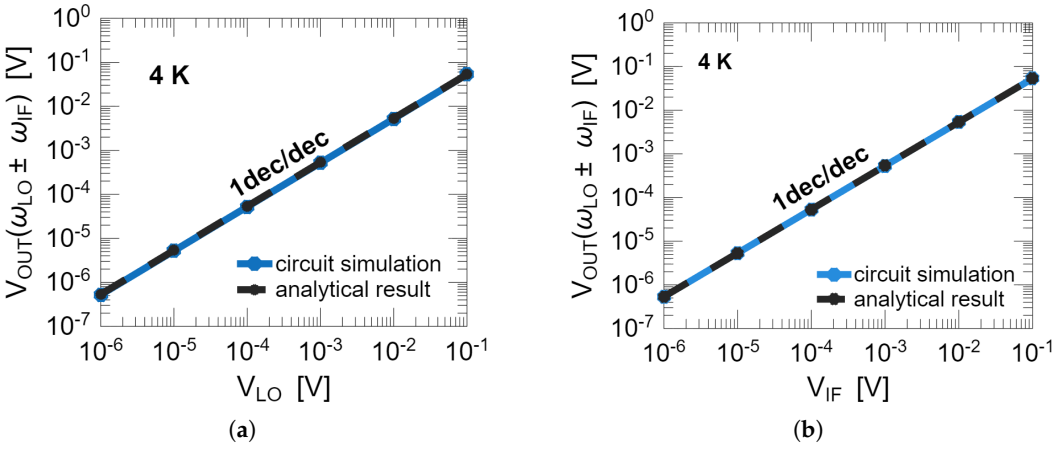


Figure 10. Amplitude of second-order intermodulation products at $\omega_{LO} \pm \omega_{IF}$ versus V_{LO} (**a**) and V_{IF} (**b**) for $V_{IF} = 100$ mV and $V_{LO} = 100$ mV, respectively, at 4 K.

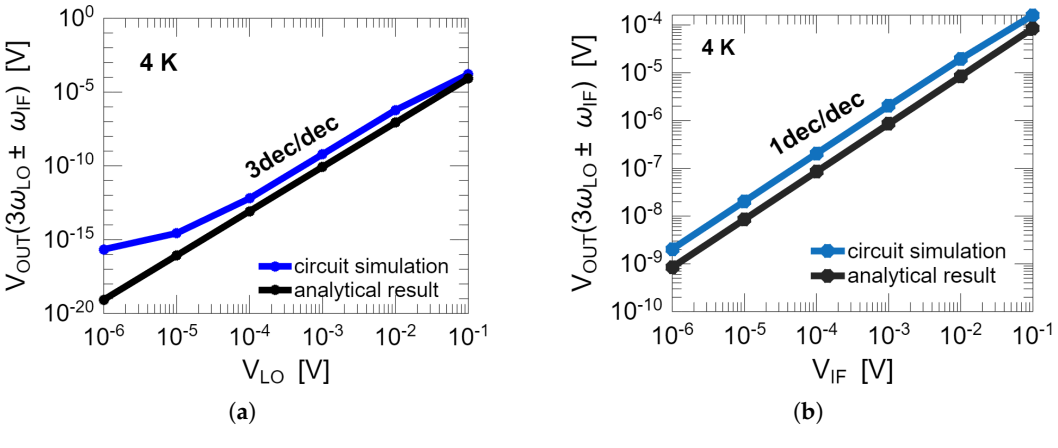


Figure 11. Amplitude of fourth-order intermodulation products at $3\omega_{LO} \pm \omega_{IF}$ versus V_{LO} (**a**) and V_{IF} (**b**) for $V_{IF} = 100$ mV and $V_{LO} = 100$ mV, respectively, at 4 K.

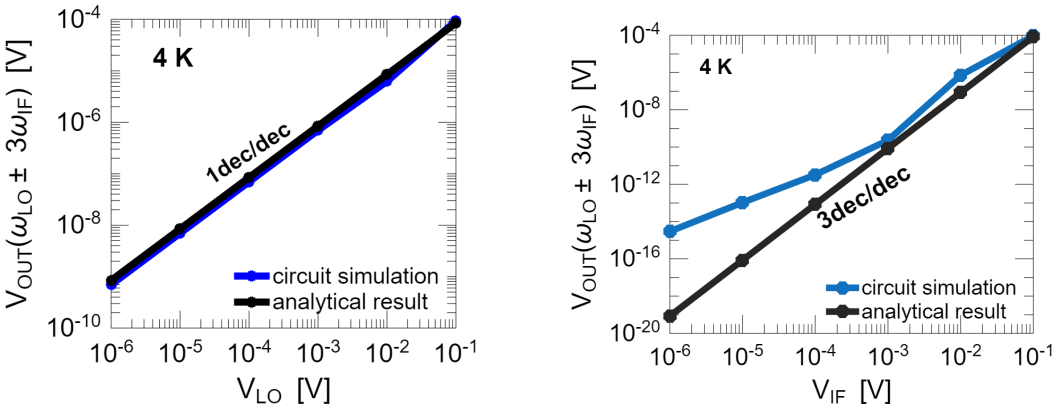


Figure 12. Amplitude of fourth-order intermodulation products at $\omega_{LO} \pm 3\omega_{IF}$ versus V_{LO} (**a**) and V_{IF} (**b**) for $V_{IF} = 100$ mV and $V_{LO} = 100$ mV, respectively, at 4 K.

Overall, the tables and figures show good agreement between calculated and simulated amplitudes. The left columns in Tables 7–14 and the curves in Figures 7 and 10 agree with Equation (73) provided by the proposed analytical model. They indeed show a linear dependence of the second-order intermodulation product amplitudes on V_{LO} and V_{IF}, with the higher orders in Equation (73) negligible, as pointed out by the other columns in the tables and by the other figures on the fourth-order intermodulation products. Similarly, the mid and right columns in the tables and the curves in Figures 8 and 9 and in Figures 11 and 12 are in agreement with the Equations (74) and (75) provided by the analytical model. In particular, in agreement with Equations (74) and (75), both at RT and CT, the simulated amplitudes of the tones at frequencies $\omega_{LO} \pm 3\omega_{IF}$ and $3\omega_{LO} \pm \omega_{IF}$, respectively, exhibit a linear dependence on the amplitude of the sweeping LO and IF, respectively, and a cubic dependence on the amplitude of the sweeping IF and LO, respectively; nevertheless, some disagreement between the analytical model and the circuit simulation has to be noted. Regardless of the temperature, when the V_{LO} (V_{IF}) sweeps, for V_{LO} (V_{IF}) lower than 10^{-4} V (10^{-3} V), we observe an error in the amplitudes at frequencies $V_{OUT}(3\omega_{LO} \pm \omega_{IF})(V_{OUT}(\omega_{LO} \pm 3\omega_{IF}))$. It seems, therefore, that when the sweeping tone (V_{LO}, V_{IF}) contributes by its third harmonic ($3\omega_{LO}$, $3\omega_{IF}$), circuit simulations are more prone to suffer from some numerical error for lower amplitudes. Indeed, when the sweeping tone contributes by its fundamental harmonic (ω_{LO}, ω_{IF}), error is no longer observed. In addition, it should be pointed out that at 4 K, for the tones at frequencies $\omega_{LO} \pm 3\omega_{IF}$ and $3\omega_{LO} \pm \omega_{IF}$, circuit simulations and analytical results appear weakly shifted. In our opinion, this can be ascribed to the fact that, for the HBT at 4 K, the exponential dependence of the collector current I_C on the base-emitter voltage V_{BE} is as follows:

$$I_C \approx I_{SC} e^{\frac{V_{BE}}{\eta V_{th}}} \tag{76}$$

on which the proposed analytical modeling is founded. Nevertheless, this relationship between I_C and V_{BE} is based on a Drift-Diffusion (DD) charge transport mechanism, while in the cryogenic HBT tunneling is dominant [57,58]. Indeed, the DD-based exponential dependence above was applied to the cryogenic HBT but at the cost of using an abnormally high value of η, which should be regarded just like a fitting parameter. This remark calls for the need for a more specific modeling for the cryogenic HBT, which moves from the microscopic tunneling-based charge transport from the emitter to the collector of the HBT. In this regard, it is worth pointing out that Bardin's PhD thesis is still a relevant reference today [65].

3.2. SFDR Analytical Evaluation

According to the definition of $SFDR$ reminded in the Introduction, its mathematical expression for a mixer is as follows:

$$SFDR = 20\log_{10}\left[\frac{A_\omega}{\max(A_{k\omega})}\right] \tag{77}$$

where A_ω is the amplitude of the desired output spectral component at frequency $\omega_{IF} \pm \omega_{LO}$, and $\max(A_{k\omega})$ is the amplitude of the highest unwanted intermodulation products, which, in the present case, are at frequencies $3\omega_{IF} \pm \omega_{LO}$ and $\omega_{IF} \pm 3\omega_{LO}$. We can thus define a couple of $SFDR$ as follows:

$$SFDR_1 = 20\log_{10}\left[\frac{V_{OUT}(\omega_{LO} \pm \omega_{IF})}{V_{OUT}(3\omega_{LO} \pm \omega_{IF})}\right] \tag{78}$$

$$SFDR_2 = 20\log_{10}\left[\frac{V_{OUT}(\omega_{LO} \pm \omega_{IF})}{V_{OUT}(\omega_{LO} \pm 3\omega_{IF})}\right] \tag{79}$$

By introducing the following constants:

$$K_1 = \frac{1}{2\eta V_{\text{th}} + R_1 I_0}\frac{I_E}{2\eta V_{\text{th}} + R_2 I_E} \tag{80}$$

$$K_2 = \frac{\eta V_{\text{th}}}{(2\eta V_{\text{th}} + R_1 I_0)^4}\frac{I_E}{2\eta V_{\text{th}} + R_2 I_E} \tag{81}$$

$$K_3 = \frac{I_E \eta V_{\text{th}}}{(2\eta V_{\text{th}} + R_2 I_E)^4}\frac{1}{2\eta V_{\text{th}} + R_1 I_0} \tag{82}$$

into Equations (73)–(75) you obtain the following:

$$V_{OUT}(\omega_{LO} \pm \omega_{IF}) = \frac{R_L}{2}K_1 V_{LO} V_{IF} - \frac{R_L}{4}K_2 V_{LO}^3 V_{IF} - \frac{R_L}{4}K_3 V_{LO} V_{IF}^3 \tag{83}$$

$$V_{OUT}(3\omega_{LO} \pm \omega_{IF}) = -\frac{R_L}{12}K_2 V_{LO}^3 V_{IF} \tag{84}$$

$$V_{OUT}(\omega_{LO} \pm 3\omega_{IF}) = -\frac{R_L}{12}K_3 V_{LO} V_{IF}^3 \tag{85}$$

The substitution of Equations (83)–(85) into Equations (78) and (79) yields the following:

$$\begin{aligned} SFDR_1 &= 20\log_{10}\left(\left|\frac{\frac{R_L}{2}K_1 V_{LO} V_{IF} - \frac{R_L}{4}K_2 V_{LO}^3 V_{IF} - \frac{R_L}{4}K_3 V_{LO} V_{IF}^3}{\frac{R_L}{12}K_2 V_{LO}^3 V_{IF}}\right|\right) = \\ &= 20\log\left[\left|6\frac{K_1}{K_2 V_{LO}^2} - 3\left(\frac{K_3 V_{IF}^2}{K_2 V_{LO}^2} + 1\right)\right|\right] \end{aligned} \tag{86}$$

$$\begin{aligned} SFDR_2 &= 20\log_{10}\left(\left|\frac{\frac{R_L}{2}K_1 V_{LO} V_{IF} - \frac{R_L}{4}K_2 V_{LO}^3 V_{IF} - \frac{R_L}{4}K_3 V_{LO} V_{IF}^3}{\frac{R_L}{12}K_3 V_{IF}^3 V_{LO}}\right|\right) = \\ &= 20\log\left|6\frac{K_1}{K_3 V_{IF}^2} - 3\left(\frac{K_2 V_{LO}^2}{K_3 V_{IF}^2} + 1\right)\right| \end{aligned} \tag{87}$$

Since from Equations (80)–(82) it results in the following:

$$\frac{K_1}{K_2} = \frac{(2\eta V_{th} + R_1 I_0)^3}{\eta V_{th}} \tag{88}$$

$$\frac{K_3}{K_2} = \frac{(2\eta V_{\text{th}} + R_1 I_0)^3}{(2\eta V_{th} + R_2 I_E)^3} \tag{89}$$

$$\frac{K_1}{K_3} = \frac{(2\eta V_{th} + R_2 I_E)^3}{\eta V_{th}} \tag{90}$$

Equations (86) and (87) can be rewritten as follows:

$$SFDR_1 = 20\log_{10}\left\{\left|6\frac{(2\eta V_{th} + R_1 I_0)^3}{\eta V_{th} V_{LO}^2} - 3\left[\frac{(2\eta V_{\text{th}} + R_1 I_0)^3 V_{IF}^2}{(2\eta V_{\text{th}} + R_2 I_E)^3 V_{LO}^2} + 1\right]\right|\right\} \tag{91}$$

$$SFDR_2 = 20\log_{10}\left\{\left|6\frac{(2\eta V_{th} + R_2 I_E)^3}{\eta V_{th} V_{IF}^2} - 3\left[\frac{(2\eta V_{\text{th}} + R_2 I_E)^3 V_{LO}^2}{(2\eta V_{\text{th}} + R_1 I_0)^3 V_{IF}^2} + 1\right]\right|\right\} \tag{92}$$

We take as $SFDR$ the worst case between $SFDR_1$ and $SFDR_2$:

$$SFDR = min(SFDR_1, SFDR_2) \tag{93}$$

Since the emitter degeneration resistors R_1 and R_2 impact the linearity, $SFDR$ has been calculated for $V_{IF} = V_{LO}$ = 100 mV by adopting the values in Tables 4–6 except for the degeneration resistors. First R_1 has been swept by keeping R_2 constant (800 Ω) and then R_2 has been swept by keeping R_1 constant (800 Ω). Figure 13a and Figure 13b depicts the obtained results at RT. The figure points out that $SFDR_1$ ($SFDR_2$), linked to intermodulation product at frequency $\omega_{IF} \pm 3\omega_{LO}$ ($3\omega_{IF} \pm \omega_{LO}$), determines the $SFDR$ for R_1 (R_2) lower than about 800 Ω, in agreement with R_1 (R_2) and ω_{LO} (ω_{IF}) being present in the first (second) section of the Gilbert multiplier. Similar results were obtained at CT.

This remark reveals that the linearity of the whole multiplier is set by the differential pair in the two sub-circuits (input differential amplifier and Gilbert cell in Figure 5) designed with the lower value of degeneration resistance. It is, therefore, reasonable to design the Gilbert multiplier with the same values of degeneration resistances, as Table 4 points out.

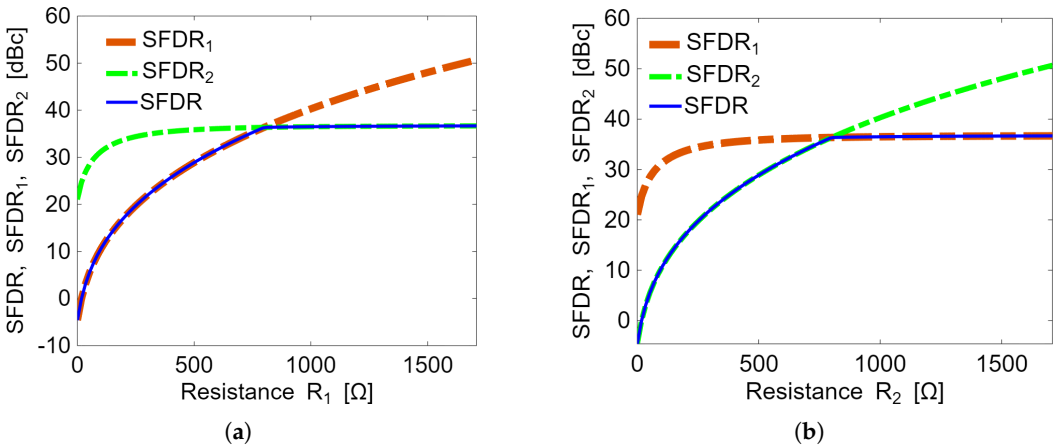


Figure 13. Analytically calculated $SFDR$ vs. R_1 (**a**) or R_2 at 300 K (**b**).

This investigation, carried out by an analytical model, has been repeated by transient simulations. Figure 14 shows good agreement between the calculated and simulated $SFDR$ at RT. Similarly, this was observed at CT, as depicted in Figure 15.

The proposed analytical model predicts the maximum value of the $SFDR$ at RT well, and it follows well the increase in $SFDR$ with the increase in the degeneration resistance at CT. Moreover, the analytical model predicts the minimum of the $SFDR$ in the same range of degeneration resistance observed in the simulated $SFDR$. Of course, being realistic, the models provided by the DK and the simulations do not reproduce the sharp minimum given by the analytical model.

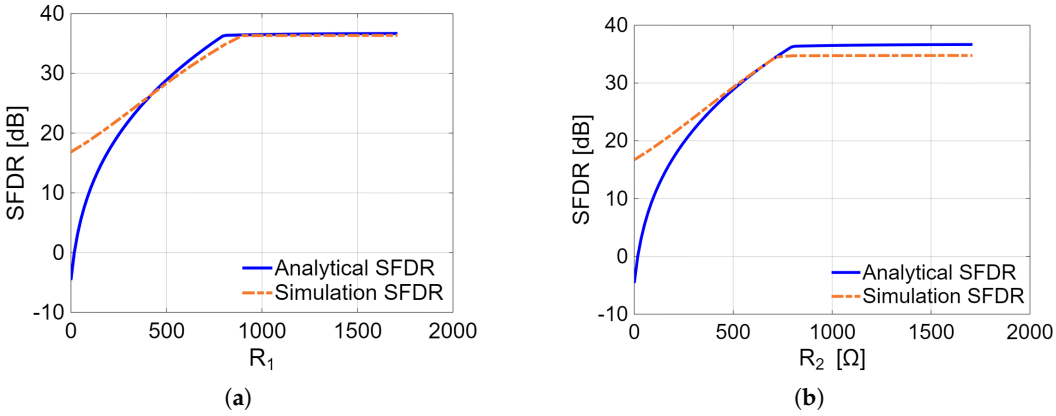


Figure 14. Analytical and simulated SFDR vs. R_1 (**a**) or R_2 at 300 K (**b**).

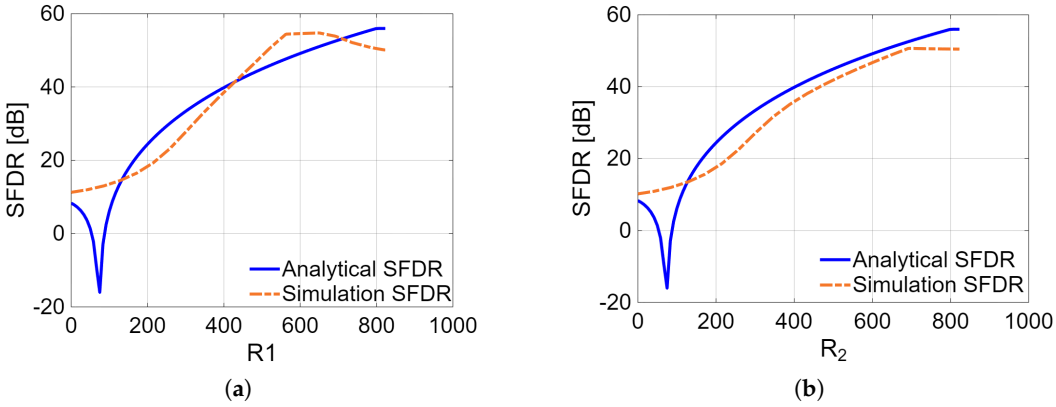


Figure 15. Analytical and simulated SFDR vs. R_1 (**a**), or vs. R_2 at 4 K (**b**).

In particular, Figures 14 and 15 show that the analytical model predicts a negative $SFDR$, that $|a_1|$ is lower than $|a_3|$, for low enough values of the degeneration resistors. Figure 13a and Figure 13b show, respectively, that in these intervals the $SFDR$ is set by $SFDR_1$ and $SFDR_2$, respectively. When R_1 sweeps while R_2 is kept constant at 800 Ω, the edge values of R_1, for which $|a_1| = |a_3|$, can be calculated straightforwardly thus from Equation (91) as follows:

$$\left[\frac{2}{\eta V_{th} V_{LO}^2} - \frac{V_{IF}^2}{y^3 V_{LO}^2}\right] x^3 = \frac{2}{3} \tag{94}$$

$$\left[\frac{2}{\eta V_{th} V_{LO}^2} - \frac{V_{IF}^2}{y^3 V_{LO}^2}\right] x^3 = \frac{4}{3} \tag{95}$$

where $x \triangleq 2\eta V_{th} + R_1 I_0$ and $y \triangleq 2\eta V_{th} + R_2 I_E$. For the values reported in Tables 4–6, Equations (94) and (95) provides the pair of edge values $R_1 \simeq -86.4\ \Omega$, $R_1 \simeq 15.9\ \Omega$ ($R_1 \simeq 53.5\ \Omega$, $R_1 \simeq 86.9\ \Omega$) at RT (CT). In addition, it is worth pointing out that Figure 15 seems to exhibit a cusp but, actually, it is the vertical asymptote corresponding to a null-valued argument of the $SFDR$. Still for R_1 sweeping and $R_2 = 800\ \Omega$, Equation (91) yields the value of R_1 positioning this asymptote:

$$\left[\frac{2}{\eta V_{th} V_{LO}^2} - \frac{V_{IF}^2}{y^3 V_{LO}^2}\right] x^3 = 1 \tag{96}$$

For the values reported in Tables 4–6. Equation (96) yields $R_1 \simeq -29.4\ \Omega$ at RT and $R_1 \simeq 72.1\ \Omega$ at CT.

When R_2 sweeps while R_1 is kept constant at 800 Ω, Equation (92) provides the edge and asymptotic values of R_2. Because of the mathematical symmetry of Equations (91) and (92), the obtained values for R_2 are identical to the previously calculated values for R_1. For the sake of exactness, it should be noted that each of Equations (94)–(96) also exhibits a couple of complex conjugate solutions, as discussed in Appendix C.

Eventually, Table 15 compares calculated and simulated $SFDR$ for degeneration resistors equal to 800 Ω. The analytical model overestimates the $SFDR$ with a relative error of about 5% (10%) at 300 K (4 K). Nevertheless, it remains clear that the analytical model is able to predict that the $SFDR$ improves by decreasing the temperature. It is worth pointing out that the SFDR values in Table 15 are, at RT, close to and, at CT, better than the benchmark value of 40 dB. This is a relevant result, because the $SFDR$ is an important parameter for the control of qubits, as the Introduction points out.

Table 15. Comparison between analytically modeled and simulated $SFDR$ for the Gilbert multiplier.

Temp. [K]	SFDR (Model)	SFDR (Simulation)
300	36.357	34.661
4	55.940	50.372

Overall, we can, therefore, close this section by concluding that the analytical model is able to size pretty well the main characteristics of the Gilbert multiplier implemented in the SG13G2 technology both under RT and CT temperature regimes.

4. Jones Demodulator

The Jones demodulator is a multiplier-based mixer, as discussed in the Introduction. The present paper addresses a BiCMOS implementation, whose generic schematic is depicted in Figure 16. The dashed rectangles point out three sections. In the switching section, the switching activity of the field-effect transistors M1 ÷ M4 generates intermodulation products of frequencies $mf_{LO} \pm nf_{IF}$ where both m and n are integer numbers. The transconductance section is made of bipolar transistors, and it is the same circuit investigated in Section 2. The load section is just constituted by a couple of resistors.

The transistors in the switching section are driven by the LO_+ and LO_- square wave signals, oscillating in antiphase at frequency f_{LO} between $0V$ and V_G. When LO_+ is high, M1 and M4 are ON, while, M2 and M3 are OFF. The current I_L (I_R) flowing through the left (right) load resistor R_L is thus I_{C1} (I_{C2}). The output differential current, defined as $\Delta I_{LR} = I_L - I_R$, is equal to $\Delta I_{12} = I_{C1} - I_{C2}$ and the differential output voltage ΔV_{OUT}, defined as $V_{OUT,R} - V_{OUT,L}$, is equal to $R_L(I_L - I_R) = R_L \Delta I_{12}$. When, instead, LO_- is high, M1 and M4 are OFF, while, M2 and M3 are ON. The current flowing through the left (right) load resistor R_L is now I_{C2} (I_{C1}). In this case $\Delta I_{LR} = I_{C2} - I_{C1} = -\Delta I_{12}$ and

$\Delta V_{OUT} = -R_L \Delta I_{12}$. The output differential voltage ΔV_{OUT} thus results in a square wave signal oscillating at frequency f_{LO} between $R_L \Delta I_{12}$ and $-R_L \Delta I_{12}$ as depicted in Figure 17.

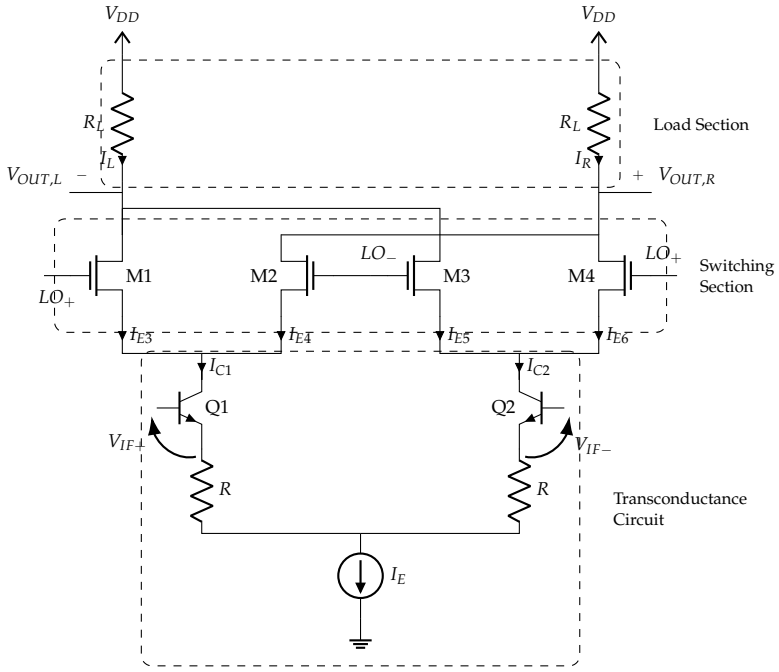


Figure 16. Generic schematic of the BiCMOS Jones demodulator.

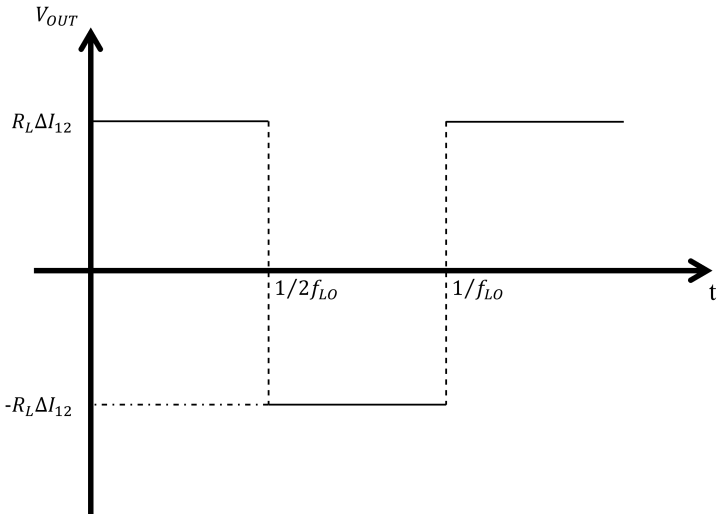


Figure 17. Differential output voltage of the Jones demodulator in the time domain.

Since it is a square wave of peak amplitude $V_{OUT,peak} \triangleq R_L \Delta I_{12}$, and frequency f_{LO}, its Fourier series is as follows:

$$\Delta V_{OUT}(t) = R_L \Delta I_{12} \frac{4}{\pi} \sum_{n=0}^{+\infty} \frac{\sin[(2n+1)\omega_{LO} t]}{(2n+1)} \tag{97}$$

Since the transconductance section, composed by Q1 and Q2, it is fed by the input differential voltage signal $\Delta V_{IN} \cos(\omega_{IF} t)$ and its behaviour can be described according to Sub-section 2.1, by reminding Equations (24)–(26) we can write the following:

$$\Delta V_{OUT}(t) = \frac{4}{\pi} R_L [a_1 \cos(\omega_{IF} t) + a_3 \cos(3\omega_{IF} t)] \left\{ \sum_{n=0}^{+\infty} \frac{\sin[(2n+1)\omega_{LO} t]}{(2n+1)} \right\} \tag{98}$$

with the following:

$$a_1 \triangleq \frac{\frac{I_E}{2\eta V_{th}}}{1+\frac{RI_E}{2\eta V_{th}}}\Delta V_{IN} - 3\frac{I_E}{96(\eta V_{th})^3}\frac{1}{\left(1+\frac{I_E R}{2\eta V_{th}}\right)^4}\Delta V_{IN}^3 \tag{99}$$

$$a_3 \triangleq -\frac{I_E}{96(\eta V_{th})^3}\frac{1}{\left(1+\frac{I_E R}{2\eta V_{th}}\right)^4}\Delta V_{IN}^3 \tag{100}$$

By recalling the trigonometric identity $2\sin(\alpha)\cos(\beta) = \sin(\alpha-\beta)+\sin(\alpha+\beta)$, Equation (98) can be rewritten as follows:

$$\Delta V_{OUT}(t) = \frac{2}{\pi}R_L a_1\left\{\sum_{n=0}^{+\infty}\frac{\sin[(2n+1)\omega_{LO}+\omega_{IF}]t}{2n+1}+\frac{\sin[(2n+1)\omega_{LO}-\omega_{IF}]t}{2n+1}\right\}+ \frac{2}{\pi}R_L a_3\left\{\sum_{n=0}^{+\infty}\frac{\sin[(2n+1)\omega_{LO}+3\omega_{IF}]t}{2n+1}+\frac{\sin[(2n+1)\omega_{LO}-3\omega_{IF}]t}{2n+1}\right\} \tag{101}$$

By limiting the series to n=1, Equation (101) provides the following second order $\Delta V_{OUT_{11}}(t)$, fourth order $\Delta V_{OUT_{13}}(t)$, $\Delta V_{OUT_{31}}(t)$ and sixth order $\Delta V_{OUT_{33}}(t)$ intermodulation products in the differential output voltage signal ΔV_{OUT}

$$\Delta V_{OUT_{11}}(t) = \frac{2}{\pi}R_L a_1 \sin[(\omega_{LO}\pm\omega_{IF})t] = \Delta V_{OUT_{11}}\sin[(\omega_{LO}\pm\omega_{IF})t] \tag{102}$$

$$\Delta V_{OUT_{13}}(t) = \frac{2}{\pi}R_L a_3 \sin[(\omega_{LO}\pm 3\omega_{IF})t] = \Delta V_{OUT_{13}}\sin[(\omega_{LO}\pm 3\omega_{IF})t] \tag{103}$$

$$\Delta V_{OUT_{31}}(t) = \frac{2}{3\pi}R_L a_1 \sin[(3\omega_{LO}\pm\omega_{IF})t] = \Delta V_{OUT_{31}}\sin[(3\omega_{LO}\pm\omega_{IF})t] \tag{104}$$

$$\Delta V_{OUT_{33}}(t) = \frac{2}{3\pi}R_L a_3 \sin[(3\omega_{LO}\pm 3\omega_{IF})t] = \Delta V_{OUT_{33}}\sin[(3\omega_{LO}\pm 3\omega_{IF})t] \tag{105}$$

From the amplitudes $\Delta V_{OUT_{11}}$, $\Delta V_{OUT_{13}}$, $\Delta V_{OUT_{31}}$, $\Delta V_{OUT_{33}}$ of these intermodulation products, it is possible to calculate the following SFDR:

$$SFDR_1 = 20\log_{10}\frac{\Delta V_{OUT_{11}}}{\Delta V_{OUT_{13}}} = 20\log_{10}\left|\frac{a_1}{a_3}\right| \tag{106}$$

$$SFDR_2 = 20\log_{10}\frac{\Delta V_{OUT_{11}}}{\Delta V_{OUT_{31}}} = 20\log_{10}3 = 9.542dB \tag{107}$$

$$SFDR_3 = 20\log_{10}\frac{\Delta V_{OUT_{11}}}{\Delta V_{OUT_{33}}} = 20\log_{10}\left|\frac{3a_1}{a_3}\right| = SFDR_1 + SFDR_2 \tag{108}$$

Equation (108) shows that, according to the definition of $SFDR$ given in Equation (93), $SFDR_3$ can be ruled out in the evaluation of the $SFDR$. On the other hand, because Equation (107) is a constant value, the $SFDR$ can not be better than 9.542 dB unless some filtering makes $SFDR_1$ the minimum, even if at the cost of renouncing the wideband feature, which may be useful in the design of a multi-frequency qubit controller [66,67].

For the sake of validation, the generic schematic in Figure 16 has been implemented in the circuit in Figure 18 using the SG13G2 technology by IHP. Table 16 reports transistor sizes, Table 17 resistances, values of the bias voltages and of the tail current, and Table 18 signal amplitudes and frequencies. Note that the dynamic of the LO signal is between 0 V and 1.6 V and large enough for making the transistors quad (M1,M2,M3,M4) behave like switches.

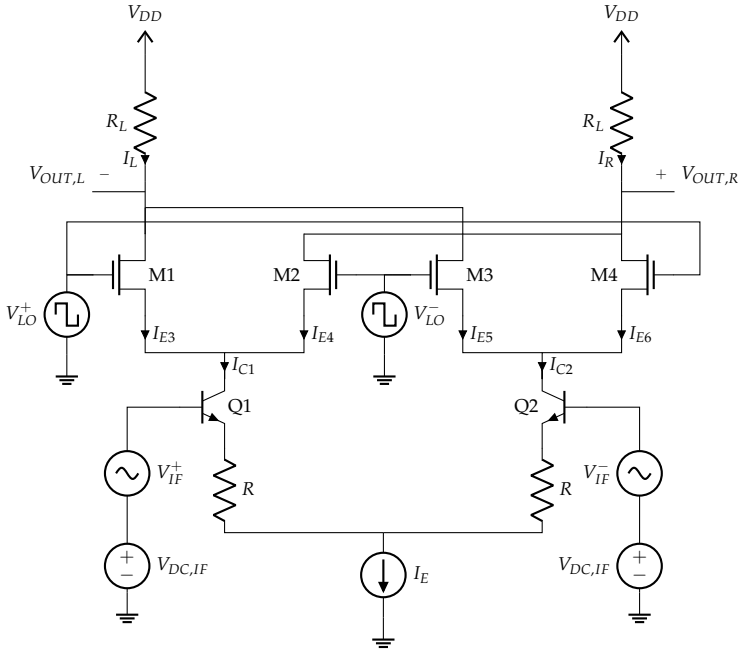


Figure 18. Jones schematic in the SG13G2 technology.

Table 16. Transistor sizes at RT and CT; n_1 set the number of gates in the field effect transistors while, m_1 the number of emitter fingers in the junction transistors.

Temp. [K]	W_{MOS} [µm]	L_{MOS} [nm]	n_1	W_{HBT} [nm]	L_{HBT} [nm]	m_1
300	12.45	130	10	70	900	1
4	12.45	130	10	70	900	1

Table 17. Resistances, bias voltages and tail current.

Temp. [K]	V_{DD} [V]	$V_{DC,IF}$ [V]	R_L [Ω]	R [Ω]	I_E [μA]
300	1.6	1.2	2000	800	117
4	1.6	1.2	2000	800	243

Table 18. Amplitudes and frequencies of the input signals.

Temp. [K]	$V_{LO,min}$ [V]	$V_{LO,max}$ [V]	V_{IF} [mV]	f_{LO} [GHz]	f_{IF} [MHz]
300	0	1.6	100	1	140
4	0	1.6	100	1	140

The substitution of these values into Equations (102)–(104) leads to the amplitudes reported in the following Table 19.

Table 19. Calculated amplitudes from the analytical model.

Temperature [K]	$\Delta V_{OUT_{11}}$ [mV]	$\Delta V_{OUT_{31}}$ [mV]	$\Delta V_{OUT_{13}}$ [mV]
300	95.362	31.787	1.387
4	144.843	48.281	0.231

On the other hand, Figure 19a,b show the spectra of the output differential voltage, for the same values as before, calculated from transient simulations.

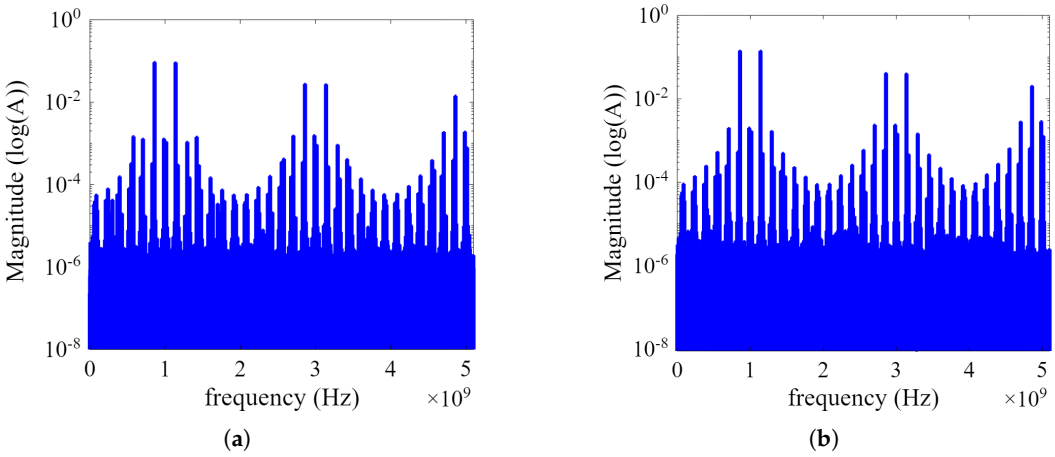


Figure 19. Output voltage spectrum of 300 K model (**a**) and 4 K (**b**).

Table 20 compares simulated and calculated amplitudes together with the corresponding relative errors. As already observed for the Gilbert multiplier, the error is more pronounced for simulations carried out at CT. Table 20 shows also that the simulated SFDR is about 10.539 dB at RT and about 10.798 dB, values 1 dB close to the 9.542 dB value predicted by the analytical model in Equation (107).

Table 20. Comparison between analytical and simulated amplitudes.

Temp. [K]	Simulated [mV]	Analytical [mV]	Err. [%]
$\Delta V_{OUT_{11}}(\omega_{LO} \pm \omega_{IF})$			
300	92.870	95.362	−2.68
4	142.406	144.843	−2.44
$\Delta V_{OUT_{13}}(\omega_{LO} \pm 3\omega_{IF})$			
300	1.433	1.387	3.20
4	0.185	0.231	−24.86
$\Delta V_{OUT_{31}}(3\omega_{LO} \pm \omega_{IF})$			
300	27.600	31.787	−15.17
4	41.079	48.281	−17.53

5. Conclusions

This work has presented a non-linear analytical modeling of a wideband bipolar Gilbert multiplier and of a BiCMOS Jones demodulator. Since both circuits can be used for frequency translation purposes, with the BiCMOS Jones demodulator being the most adopted circuit solution nowadays, and since the aim of this paper is the analytical modeling of non-linear behaviors, the investigation was mainly focused on the generation of intermodulation products. As the two circuits share the same degenerated bipolar transistor pair, this pair has been modelled first; MOSFET were used only for the switching section of the Jones demodulator. The following investigation approach has been the same for all investigated circuits (degenerated transistor pair, Gilbert multiplier, and Jones demodulator): first, the analytical model was developed for a generic schematic, and then it was validated by comparing its predictions with Cadence circuit simulations carried out on the circuit obtained by implementing the generic schematic into the 130 nm BiCMOS technology SG13G2 by IHP. It is worth noting that the device models offered by a design kit are obtained by the foundry from experimental data; for the microelectronics designer, the device models in a design kit thus have the same credibility/reliability as an experimental

characterization. Since the design kit for the SG13G2 technology offers not only room temperature but also cryogenic model cards of active and passive devices, all addressed circuits have been investigated both at room and cryogenic temperatures. The circuits have, therefore, been designed twice, and the simulations have been compared with the model predictions. Overall, the model demonstrated to be in good agreement with the simulations under both temperature regimes. The proposed analytical model is able to reproduce, on its own, that is, without any fitting procedure other than that related to the non-ideality coefficient η in the Gummel plots, the behavior of the simulated amplitudes of the second- and fourth-order intermodulation products with the exception of the tones at $3\omega_{LO} \pm \omega_{IF}$, for which the model predictions are optimistic with respect to the simulations. It is the authors' opinion that this has to be ascribed to the adoption of the DD physically based exponential $I_C - V_{BE}$ characteristic for the HBT at 4 K, while, on the other hand, the dominant charge transport mechanism at cryogenic temperature is trap-assisted tunneling. In this framework, the non-ideality factor η is just a fitting parameter. This points out the need for more specific modeling of the cryogenic HBT $I_C - V_{BE}$ characteristic. To this end, optimization algorithms can come into play by using the non-ideality factor η as a relevant parameter [23]-[26].

As far as the $SFDR$, the discrepancy between analytical predictions and simulations is, regardless of temperature, lower than 10%, which has to be considered as a good agreement. In particular, it is worth pointing out that the SFDR at 4 K was found to be in the range of 50 dB, a value well aligned with the performance claimed in the literature [7,31,39,61] for controllers for semiconductor spin and transmon qubits. For the Jones demodulator, the proposed analytical model agrees with the Cadence simulations that a wideband Jones demodulator cannot offer an SFDR better than about 10 dB, regardless of temperature. Since $SFDR$ is a figure-of-merit assessing the spectral purity of the output signal generated by the multiplier, this finding is very interesting, because it suggests the Gilbert multiplier as an interesting potential mixer for cryogenic circuits for quantum computing as qubit controllers or demodulators for reflectometric qubit readout. This conclusion invites to explore systematically the use of a Gilbert multiplier in cryogenic circuits for quantum computing cryogenic BiCMOS circuitry.

In addition, the overall satisfying agreement between the non-linear analytical model and the circuit simulations obtained both for the Gilbert multiplier and the Jones modulator points out that the analytical equations provided by the proposed analytical model can be assumed as design equations helpful for designing a wideband mixer for a given $SFDR$ target even under cryogenic temperature conditions.

Author Contributions: Conceptualization, M.B. (Matteo Biscolli) and M.B. (Mattia Borgarino); methodology, M.B. (Matteo Biscolli) and M.B. (Mattia Borgarino); software, M.B. (Matteo Biscolli); validation, M.B. (Matteo Biscolli) and M.B. (Mattia Borgarino); formal analysis, M.B. (Matteo Biscolli) and M.B. (Mattia Borgarino); investigation, M.B. (Matteo Biscolli); writing—original draft preparation, M.B. (Matteo Biscolli); writing—review and editing, M.B. (Mattia Borgarino); visualization, M.B. (Matteo Biscolli); supervision, M.B. (Mattia Borgarino). All authors have read and agreed to the published version of the manuscript.

Funding: This research received no external funding

Institutional Review Board Statement: Not applicable.

Informed Consent Statement: Not applicable.

Data Availability Statement: Data is contained within the article.

Acknowledgments: The authors would like to thank the IHP foundry (Frankfurt am Oder, Germany) for having provided the cryogenic Design Kit of the SiGe 130 nm BiCMOS technology SG13G2C.

Conflicts of Interest: The authors declare no conflicts of interest.

Abbreviations

The following abbreviations are used in this manuscript:

CT	Cryogenic Temperature
CVTC	Current–Voltage Transfer Characteristics
DD	Drift-Diffusion
DFT	Discrete Fourier Transform
DK	Design Kit
HBT	Heterojunction Bipolar Transistor
RT	Room Temperature
SFDR	Spurious-Free Dynamic Range

Appendix A. Calculations of the Derivatives

Appendix A.1. First Derivative $\left.\frac{d\Delta I_{OUT}}{d\Delta V_{IN}}\right|_{V_{IN}=0}$

From Equation (14), after having defined $u = \frac{\Delta V_{IN} - R\Delta I_{OUT}}{2\eta V_{th}}$ we obtained the following:

$$\frac{d\Delta I_{OUT}}{d\Delta V_{IN}} = I_0 \frac{d\tanh(u)}{du}\frac{du}{d\Delta V_{IN}} \tag{A1}$$

From the definition of u we obtain the following:

$$\frac{du}{d\Delta V_{IN}} = \frac{d\frac{\Delta V_{IN} - R\Delta I_{OUT}}{2\eta V_{th}}}{d\Delta V_{IN}} = \frac{1}{2\eta V_{th}}\frac{d(\Delta V_{IN} - R\Delta I_{OUT})}{d\Delta V_{IN}} = \frac{1}{2\eta V_{th}}\left(1 - R\frac{d\Delta I_{OUT}}{d\Delta V_{IN}}\right) \tag{A2}$$

Substituting Equation (A2) into Equation (A1) we obtained the following:

$$\frac{d\Delta I_{OUT}}{d\Delta V_{IN}} = \frac{I_0}{2\eta V_{th}}\frac{d\tanh(u)}{du}\left(1 - R\frac{\Delta I_{OUT}}{d\Delta V_{IN}}\right) \tag{A3}$$

and by reminding that $\frac{d\tanh(u)}{du} = \mathrm{sech}^2(u)$:

$$\frac{d\Delta I_{OUT}}{d\Delta V_{IN}} = \frac{I_0}{2\eta V_{th}}\mathrm{sech}^2(u)\left(1 - R\frac{d\Delta I_{OUT}}{d\Delta V_{IN}}\right) \tag{A4}$$

which, once solved for $\frac{d\Delta I_{OUT}}{d\Delta V_{IN}}$, provides the following:

$$\frac{d\Delta I_{OUT}}{d\Delta V_{IN}} = \frac{\frac{I_0}{2\eta V_{th}}\mathrm{sech}^2(u)}{\left(1 + R\frac{I_0}{2\eta V_{th}}\mathrm{sech}^2(u)\right)} \tag{A5}$$

Since $\Delta I_{OUT} = 0$ for $\Delta V_{IN} = 0$, as pointed out above, from the definition of $u = \frac{\Delta V_{IN} - R\Delta I}{2\eta V_{th}}$ leads to $u = 0$. For $\Delta V_{IN} = 0$ we obtain the following:

$$\left.\frac{d\Delta I_{OUT}}{d\Delta V_{IN}}\right|_{\Delta V_{IN}=0} = \frac{I_0}{2\eta V_{th}}\frac{\mathrm{sech}^2(u)}{\left(1 + R\frac{I_0}{2\eta V_{th}}\mathrm{sech}^2(u)\right)} = \frac{\frac{I_0}{2\eta V_{th}}}{1 + \frac{RI_0}{2\eta V_{th}}} \tag{A6}$$

where it has been reminded that $\mathrm{sech}(0) = 1$

Appendix A.2. Second Derivative $\left.\frac{d^2\Delta I_{OUT}}{d\Delta V_{IN}^2}\right|_{V_{IN}=0}$

The second derivative of Equation (14) is the first derivative of Equation (A5). So we can derive Equation (A5) further. We start by calculating the derivative of $\text{sech}^2(u)$, by reminding that $u = \frac{\Delta V_{IN} - R\Delta I_{OUT}}{2\eta V_{th}}$:

$$\frac{d}{d\Delta V_{IN}}\text{sech}^2\left(\frac{\Delta V_{IN} - R\Delta I_{OUT}}{2\eta V_{th}}\right) = -2\,\text{sech}^2\left(\frac{\Delta V_{IN} - R\Delta I_{OUT}}{2\eta V_{th}}\right)\tanh\left(\frac{\Delta V_{IN} - R\Delta I_{OUT}}{2\eta V_{th}}\right)\frac{1 - R\frac{d\Delta I_{OUT}}{d\Delta V_{IN}}}{2\eta V_{th}} \tag{A7}$$

Now by rewriting Equation(A5) and substituting $\frac{I_0}{2V_{th}}\text{sech}^2\left(\frac{\Delta V_{IN} - R\Delta I_{OUT}}{2\eta V_{th}}\right)$ with A, where $A^{(1)}$ denotes the first derivative, we obtain the following equation:

$$\frac{d}{d\Delta V_{IN}}\left(\frac{A}{1+RA}\right) = \frac{A^{(1)}(1+RA) - RA^{(1)}A}{(1+RA)^2} = \frac{A^{(1)}}{(1+RA)^2} \tag{A8}$$

But $A^{(1)}$ is equal to Equation(A7), so you obtain the following:

$$\frac{A^{(1)}}{(1+RA)^2} = \frac{I_0\left(1 - R\frac{d\Delta I_{OUT}}{d\Delta V_{IN}}\right)}{(2\eta V_{th})^2}\frac{-2\,\text{sech}^2\left(\frac{\Delta V_{IN} - R\Delta I_{OUT}}{2\eta V_{th}}\right)\tanh\left(\frac{\Delta V_{IN} - R\Delta I_{OUT}}{2\eta V_{th}}\right)}{\left[1 + \frac{RI_0}{2\eta V_{th}}\text{sech}^2\left(\frac{\Delta V_{IN} - R\Delta I_{OUT}}{2\eta V_{th}}\right)\right]^2} \tag{A9}$$

In this equation it is present the term $\frac{d\Delta I_{OUT}}{d\Delta V_{IN}}$, that we can substitute with the Equation (A5) to obtain the following:

$$\begin{aligned}\frac{d^2\Delta I_{OUT}}{d\Delta V_{IN}^2} &= \left[1 - R\frac{\frac{I_0}{2\eta V_{th}}\text{sech}^2\left(\frac{\Delta V_{IN} - R\Delta I_{OUT}}{2\eta V_{th}}\right)}{1 + \frac{RI_0}{2\eta V_{th}}\text{sech}^2\left(\frac{\Delta V_{IN} - R\Delta I_{OUT}}{2\eta V_{th}}\right)}\right]\frac{-2I_0\,\text{sech}^2\left(\frac{\Delta V_{IN} - R\Delta I_{OUT}}{2\eta V_{th}}\right)\tanh\left(\frac{\Delta V_{IN} - R\Delta I_{OUT}}{2\eta V_{th}}\right)}{(2\eta V_{th})^2\left[1 + \frac{RI_0}{2\eta V_{th}}\text{sech}^2\left(\frac{\Delta V_{IN} - R\Delta I_{OUT}}{2\eta V_{th}}\right)\right]^2} \\ &= \frac{I_0}{(2\eta V_{th})^2}\frac{-2\,\text{sech}^2\left(\frac{\Delta V_{IN} - R\Delta I_{OUT}}{2\eta V_{th}}\right)\tanh\left(\frac{\Delta V_{IN} - R\Delta I_{OUT}}{2\eta V_{th}}\right)}{\left[1 + \frac{RI_0}{2\eta V_{th}}\text{sech}^2\left(\frac{\Delta V_{IN} - R\Delta I_{OUT}}{2\eta V_{th}}\right)\right]^3}\end{aligned} \tag{A10}$$

Since, for a continuity principle applied to R, the $\Delta I_{OUT} = \Delta I_{OUT}(\Delta V_{IN})$ curve is expected to exhibit an odd symmetry around the origin as it is for the curve plotted for $R = 0$, the tanh term in the numerator forces this equation to be zero for $\Delta V_{IN} = 0$.

Appendix A.3. Third Derivative $\left.\frac{d^3\Delta I_{OUT}}{d\Delta V_{IN}^3}\right|_{V_{IN}=0}$

Starting from the Equation (A10), we can substitute the following parameters:

$$u = \frac{\Delta V_{IN} - R\Delta I_{OUT}}{2\eta V_{th}}, \qquad Z = \frac{d^2\Delta I_{OUT}}{d\Delta V_{IN}^2}. \qquad \frac{du}{d\Delta V_{IN}} = \frac{d}{d\Delta V_{IN}}\left(\frac{\Delta V_{IN} - R\Delta I_{OUT}}{2\eta V_{th}}\right) \tag{A11}$$

This allows us rewriting the third derivative easily in terms of the second derivative. The third derivative is $\frac{d^3\Delta I_{OUT}}{d\Delta V_{IN}^3} = \frac{dZ}{du}\frac{du}{d\Delta V_{IN}}$. We can also define:

$$F_1 = \text{sech}^2(u)\,\tanh(u), \qquad F_2 = \left(1 + \frac{I_0 R}{2\eta V_{th}}\text{sech}^2(u)\right)^{-3} \tag{A12}$$

so that $Z = -\frac{I_0}{2\eta V_{th}^2} F_1 F_2$. Applying the product rule, the third derivative takes the following form:

$$\frac{dZ}{du} = -\frac{I_0}{2\eta V_{th}^2}\left(\frac{dF_1}{du}\frac{du}{d\Delta V_{IN}} F_2 + F_1 \frac{dF_2}{du}\frac{du}{d\Delta V_{IN}}\right). \tag{A13}$$

Using the chain rule and recalling from Equation (A7) the derivative of $\mathrm{sech}^2(u)$:

$$\frac{dF_1}{d\Delta V_{IN}} = \frac{d}{d\Delta V_{IN}}\left[\mathrm{sech}^2(u)\tanh(u)\right] = \left[-2\,\mathrm{sech}^2(u)\tanh^2(u) + \mathrm{sech}^4(u)\right]\frac{du}{d\Delta V_{IN}}. \tag{A14}$$

As far as F_2, with $G(u) = 1 + \frac{I_0 R}{2\eta V_{th}}\mathrm{sech}^2(u)$, you have $F_2 = [G(u)]^{-3}$, and thus:

$$\begin{aligned}\frac{dF_2}{d\Delta V_{IN}} &= -3[G(u)]^{-4}\frac{dG}{d\Delta V_{IN}} = \\ &= 3\frac{I_0 R}{V_{th}}\,\mathrm{sech}^2(u)\tanh(u)\,\frac{du}{d\Delta V_{IN}}\,[G(u)]^{-4}.\end{aligned} \tag{A15}$$

From Equation (A11) and substituting also Equation (A5):

$$\begin{aligned}\frac{du}{d\Delta V_{IN}} &= \frac{1}{2\eta V_{th}}\frac{1}{1 + \frac{I_0 R}{2\eta V_{th}}\mathrm{sech}^2(u)} = \\ &= \frac{1}{2\eta V_{th}}[G(u)]^{-1}\end{aligned} \tag{A16}$$

Substituting into the product rule expression and factoring $\frac{du}{d\Delta V_{IN}}$ with the denominator $[G(u)]^{-5}$:

$$\begin{aligned}\frac{dZ}{d\Delta V_{IN}} = -\frac{I_0}{2\eta V_{th}^2}\frac{du}{d\Delta V_{IN}}[G(u)]^{-4}\Bigg\{&\left[-2\,\mathrm{sech}^2(u)\tanh^2(u) + \mathrm{sech}^4(u)\right]G(u) \\ &+ 3\frac{I_0 R}{V_{th}}\,\mathrm{sech}^4(u)\tanh^2(u)\Bigg\}.\end{aligned} \tag{A17}$$

The replacement of $\frac{du}{d\Delta V_{IN}}$ cancels one factor of $G(u)$ in the denominator, leaving:

$$\frac{dZ}{d\Delta V_{IN}} = -\frac{I_0}{4(\eta V_{th})^3}[G(u)]^{-5}\left\{\left[-2\,\mathrm{sech}^2(u)\tanh^2(u) + \mathrm{sech}^4(u)\right]G(u) + 3\frac{I_0 R}{V_{th}}\,\mathrm{sech}^4(u)\tanh^2(u)\right\}. \tag{A18}$$

By expanding the bracket and gathering $\mathrm{sech}^4(u)\tanh^2(u)$:

$$\begin{aligned}&= \left(-2\,\mathrm{sech}^2(u)\tanh^2(u) + \mathrm{sech}^4(u)\right)\left(1 + \frac{I_0 R}{2\eta V_{th}}\mathrm{sech}^2(u)\right) + 3\frac{I_0 R}{V_{th}}\,\mathrm{sech}^4(u)\tanh^2(u) \\ &= -2\,\mathrm{sech}^2(u)\tanh^2(u) + \mathrm{sech}^4(u) + 2\frac{I_0 R}{V_{th}}\,\mathrm{sech}^4(u)\tanh^2(u) + \frac{I_0 R}{2\eta V_{th}}\,\mathrm{sech}^6(u).\end{aligned} \tag{A19}$$

Multiplying through by the minus sign:

$$\frac{d^3(\Delta I_{OUT})}{d\Delta V_{IN}^3} = \frac{I_0}{4(\eta V_{th})^3}\frac{2\,\mathrm{sech}^2(u)\tanh^2(u) - \mathrm{sech}^4(u) - 2\frac{I_0 R}{V_{th}}\,\mathrm{sech}^4(u)\tanh^2(u) - \frac{I_0 R}{2\eta V_{th}}\,\mathrm{sech}^6(u)}{\left(1 + \frac{I_0 R}{2\eta V_{th}}\,\mathrm{sech}^2(u)\right)^5} \tag{A20}$$

with

$$u = \frac{\Delta V_{IN} - R\Delta I_{OUT}}{2\eta V_{th}}. \tag{A21}$$

Eventually, after having put in explicit form:

$$\begin{aligned}\frac{d^3(\Delta I_{OUT})}{d\Delta V_{IN}^3} = &-\frac{I_0}{4(\eta V_{th})^3}\frac{2\,\mathrm{sech}^2\left(\frac{\Delta V_{IN} - R\Delta I_{OUT}}{2\eta V_{th}}\right)\tanh^2\left(\frac{\Delta V_{IN} - R\Delta I_{OUT}}{2\eta V_{th}}\right) - \mathrm{sech}^4\left(\frac{\Delta V_{IN} - R\Delta I_{OUT}}{2\eta V_{th}}\right)}{\left(1 + \frac{I_0 R}{2\eta V_{th}}\,\mathrm{sech}^2\left(\frac{\Delta V_{IN} - R\Delta I_{OUT}}{2\eta V_{th}}\right)\right)^5} \\ &-\frac{I_0}{4(\eta V_{th})^3}\frac{2\frac{I_0 R}{V_{th}}\,\mathrm{sech}^4\left(\frac{\Delta V_{IN} - R\Delta I_{OUT}}{2\eta V_{th}}\right)\tanh^2\left(\frac{\Delta V_{IN} - R\Delta I_{OUT}}{2\eta V_{th}}\right) + \frac{I_0 R}{2\eta V_{th}}\,\mathrm{sech}^6\left(\frac{\Delta V_{IN} - R\Delta I_{OUT}}{2\eta V_{th}}\right)}{\left(1 + \frac{I_0 R}{2\eta V_{th}}\,\mathrm{sech}^2\left(\frac{\Delta V_{IN} - R\Delta I_{OUT}}{2\eta V_{th}}\right)\right)^5}\end{aligned} \tag{A22}$$

we can calculate the third derivative for $\Delta V_{IN} = 0$ as follows:

$$\begin{aligned}\frac{1}{6}\frac{d^3\Delta I_{OUT}}{dV_{IN}^3}\bigg|_{\Delta V_{IN}=0} &= -\frac{I_0}{4(3!)(\eta V_{th})^3}\frac{1 + \frac{I_0 R}{2\eta V_{th}}}{\left(1 + \frac{I_0 R}{2\eta V_{th}}\right)^5} \\ &= -\frac{I_0}{24(\eta V_{th})^3}\frac{1}{\left(1 + \frac{I_0 R}{2\eta V_{th}}\right)^4}\end{aligned} \tag{A23}$$

Appendix B. Calculation of $V_{IN,knee}$

It is possible to estimate the input differential voltage ΔV_{IN} corresponding to the maximum output differential current ΔI_{OUT}.

To derive this value, Equation (18) can be used, as it represents the slope of the tangent at the origin. The tangent Equation is given by the following:

$$\Delta I_{OUT} = \frac{\frac{I_0}{2\eta V_{th}}}{1 + \frac{RI_0}{2\eta V_{th}}}\Delta V_{IN} \tag{A24}$$

The maximum value of ΔI_{OUT} is obtained when $\Delta I_{OUT} = I_0$. By substituting this condition into the previous Equation and solving for ΔV_{IN}, the following result is obtained:

$$\begin{aligned} I_0 &= \frac{\frac{I_0}{2\eta V_{th}}}{1 + \frac{RI_0}{2\eta V_{th}}}\Delta V_{IN_{\mathrm{knee}}} \\ 1 &= \frac{\frac{1}{2\eta V_{th}}}{1 + \frac{RI_0}{2\eta V_{th}}}\Delta V_{IN_{\mathrm{knee}}} \\ \Delta V_{IN_{\mathrm{knee}}} &= \frac{1 + \frac{RI_0}{2\eta V_{th}}}{\frac{1}{2\eta V_{th}}} = 2\eta V_{th} + RI_0 \end{aligned} \tag{A25}$$

The quantity $\Delta V_{IN_{\text{knee}}}$, therefore, corresponds to the input differential voltage for which ΔI_{OUT} reaches its maximum value, according to the first-order Taylor approximation of the curve.

Appendix C. About Complex Solutions in Equations (94)–(96)

Equations (94)–(96) can be put in the generic form $y^3 - k = 0$ with $k > 0$. According to the Fundamental Theorem of Algebra, first stated by Albert Girard (1595–1632) in 1629 [68], the equation has three solutions. Nevertheless, already in 1545 Gerolamo Cardano (1501–1576) proved that a cubic algebraic equation has one real solution and two further solutions that may be complex [69]. With reference to a cubic equation in the form $y^3 + py + q = 0$, known as the depressed one, Cardano classifies different solutions on the basis of the quantity $\Delta \triangleq \frac{q^2}{4} + \frac{p^3}{27}$. In our case, the depressed cubic equation simplifies further into $y^3 + q = 0$ with $q = -k < 0$ and the quantity Δ reduces to $\frac{q^2}{4}$, which is a positive number. Under this conditions, according to Cardano, the real solution y_1 is $-\sqrt[3]{q} = \sqrt[3]{k}$, corresponding to the values of R_1 calculated from Equations (94)–(96), while the two complex solutions y_2 and y_3 are $\sqrt[3]{k}\left(-\frac{1}{2} \pm j\frac{\sqrt{3}}{2}\right)$; note indeed that $\left(-\frac{1}{2} \pm j\frac{\sqrt{3}}{2}\right)^3 = 1$.

References

1. Razavi, B. *RF Microelectronics*, 2nd ed.; Prentice Hall: Upper Saddle River, NJ, USA, 2012; ISBN 978-0137134731.
2. Gao, Z.; Liang, C.; Liang, R.; Gan, S.; Tang, B.; Dong, X.; Zhao, Y.; Xin, Y.; Zhang, B.; Geng, L. A cryo-tolerant >40-dB IRR, 4.7–7.9-GHz double-quadrature Cryo-CMOS receiver with a broadband LNA for scalable quantum applications. *IEEE Trans. Very Large Scale Integr. (VLSI) Syst.* **2025**, *34*, 83–92. https://doi.org/10.1109/TVLSI.2025.3600894.
3. Kwende, R.C.; Rosenstock, D.; Wang, C.; Bardin, J.C. Design and characterization of a 6-mW cryogenic SiGe IC for superconducting qubit readout. *IEEE Trans. Microw. Theory Tech.* **2025**, *73*, 234–244. https://doi.org/10.1109/TMTT.2024.3456111.
4. Peng, Y.; Benserhir, J.; Zou, Y.; Charbon, E. A cryogenic double-IF SSB controller with image suppression and on-chip filtering implemented in 130-nm SiGe BiCMOS technology for superconducting qubit control. In Proceedings of the IEEE Custom Integrated Circuits Conference (CICC), Denver, CO, USA, 21–24 April 2024. https://doi.org/10.1109/CICC60959.2024.10528967.
5. Altuner, E.; Özoğuz, I.S.; Yelten, M.B. High-linearity Gilbert-cell mixer design for cryogenic applications. *Analog Integr. Circuits Signal Process.* **2022**, *113*, 249–256. https://doi.org/10.1007/s10470-022-02098-9.
6. Prabowo, B.; Pietx-Casas, O.; Montazerolghaem, M.A.; Scappucci, G.; Vandersypen, L.M.K.; Sebastiano, F.; Babaie, M. A Cryo-CMOS receiver with 15K noise temperature achieving 9.8-dB SNR in 10-μs integration time for spin qubit readout. In Proceedings of the IEEE International Solid-State Circuits Conference (ISSCC), San Francisco, CA, USA, 18–22 February 2024. https://doi.org/10.1109/ISSCC49657.2024.10454300.
7. Chakraborty, S.; Tien, K.; Frolov, D.; Frank, D.; Rosno, P.; Yeck, M.; Bulzacchelli, J.; Baks, C.; Richetta, R.; Schmerbeck, T.; et al. A 12.8-mW/channel cryogenic RF-AWG in 14-nm FinFET for transmon qubit control. In Proceedings of the European Solid-State Electronics Research Conference (ESSERC), Bruges, Belgium, 9–12 September 2024. https://doi.org/10.1109/ESSERC62670.2024.10719526.
8. Lee, T. *The Design of CMOS Radio-Frequency Integrated Circuits*, 2nd ed.; Cambridge University Press: Cambridge, UK, 2003; ISBN 978-0521835398.
9. Borgarino, M.; Badiali, A. Quantum Gates for Electronics Engineers. *Electronics* **2023**, *12*, 4664. https://doi.org/10.3390/electronics12224664.
10. Borgarino, M.; Badiali, A. Demystyfing Quantum Gate Fidelity for Electronics Engineers. *Appl. Sci.* **2025**, *15*, 2675. https://doi.org/10.3390/app15052675.
11. Gilbert, B. A high-performance monolithic multiplier using active feedback. *IEEE J. Solid-State Circuits* **1974**, *9*, 364–373. https://doi.org/10.1109/JSSC.1974.1050529.
12. Danesh, M.; Jayaraj, A.; Chandrasekaran, S.T.; Sanyal, A. Ultra-Low Power Analog Multiplier Based on Translinear Principle. In Proceedings of the IEEE International Symposium on Circuits and Systems (ISCAS), Sapporo, Japan, 26–29 May 2019; pp. 1–4. https://doi.org/10.1109/ISCAS.2019.8702330.
13. Jasielski, J.; Kuta, A.; Machowski, W.; Koáodziejski, W. Four-Quadrant CMOS Transconductance Multiplier Operating at Low Voltage and High-Speed. In Proceedings of the IEEE International Conference on Mixed Design of Integrated Circuits and Systems (MIXDES), Warsaw, Poland, 24–26 June 2010; pp. 265–268.

14. Weger, P.; Schultes, G.; Treitinger, L.; Bertagnolli, E.; Ehinger, K. Gilbert multiplier as an active mixer with conversion gain bandwidth of up to 17 GHz. *Electron. Lett.* **1991**, *27*, 7. https://doi.org/10.1049/el:19910359.
15. Tsai, M.D.; Lin, C.S.; Wang, C.H.; Lien, C.H.; Wang, H. A 0.1–23 GHz SiGe BiCMOS Analog Multiplier and Mixer Based on Attenuation-Compensation Technique. In Proceedings of the IEEE Radio Frequency Integrated Circuits Symposium, Fort Worth, TX, USA, 6–8 June 2004; pp. 417–420. https://doi.org/10.1109/RFIC.2004.1320639.
16. Lee, T.H. Tales of the Continuum: A Subsampled History of Analog Circuits. *IEEE Solid-State Circuits News* **2007**, *12*, 38–51. https://doi.org/10.1109/N-SSC.2007.4785653.
17. Jones, H.E. Dual Output Synchronous Detector, Utilizing Transistorized Differential Amplifiers. U.S. Patent 3,241,078, 8 June 1963.
18. Choma, J. A Three-Level Broad-Banded Monolithic Analog Multiplier. *IEEE J. Solid-State Circuits* **1981**, *SC-16*, 392–399. https://doi.org/10.1109/JSSC.1981.1051607.
19. Atti, M.T.A. Improved analysis of the nonlinear distorion performance of an N-level analog multiplier. *Microelectron. J.* **1981**, *22*, 89–100. https://doi.org/10.1016/0026-2692(91)90056-S.
20. Kuntman, H.H. Simple and accurate nonlinear analogue multiplier macromodel. In Proceedings of the IEEE Mediterranean Electrotechnical Conference, Tel-Aviv, Israel, 18–20 May 1998; pp. 585–589. https://doi.org/10.1109/MELCON.1998.692495.
21. Kimura, K. Bipolar Translinear Four Quadrant Analog Multiplier. U.S. Patent 5,912,834, 1999.
22. Herath, H.M.V.R.; Wimalarathna, G.H.I. An Eight-Octant bipolar junction transistor analog multiplier circuit and its applications. *Ceylon J. Sci.* **2018**, *47*, 143–151. https://doi.org/10.4038/cjs.v47i2.7510.
23. Ökten, I. A novel DIO optimized sigmoid-activated 2DOF-PID controller for robust control of magnetic levitation systems. *Sci. Rep.* 2026, 16, 27098. https://doi.org/10.1038/s41598-026-61762-6.
24. Izci, D.; Ekinci, S.; Ökten, I.; Tümen, V.; Rashdan, M.; Salman, M. A Schrödinger and differential evolution framework for PID based liquid level control. *Sci. Rep.* **2026**, *16*, 30889. https://doi.org/10.1038/s41598-026-68734-w.
25. Tümen, V.; Elmastas, N.; Ökten, I.; Ekinci, S.; Izci, D.; Rashdan, M.; Salman, M. A discrete enzyme action optimizer for traveling salesman problems with a smart tourism routing application: A case study in Bitlis, Türkiye. *Sci. Rep.* **2026**, *16*, 27433. https://doi.org/10.1038/s41598-026-56861-3.
26. Kochenderfer, M.J.; Wheeler, T.A. *Algorithms for Optimization*; The MIT Press: Cambridge, MA, USA, 1st Edition 2019, ISBN 978-0262039420, 2nd Edition, Jan. 2027, ISBN 9780262058162.
27. Kapoulea, S. Cryo-CMOS ICs for Scalable Quantum Computing. In *Advanced Circuits and Systems: From Theory to Emerging Applications*; River Publishers: Aalborg, Denmark, 2026; pp. 163–180, ISBN 9788743812777.
28. Sebastiano, F. Fundamentals of Cryo-CMOS Circuits and Systems for Quantum Computing. *IEEE Solid-State Circuits Mag.* **2025**, *17*, 61–71. https://doi.org/10.1109/MSSC.2025.3581166.
29. Chakraborty, S.; Joshi, R.V. Cryogenic CMOS Design for Qubit Control: Present Status, Challenges, and Future Directions. *IEEE Circuits Syst. Mag.* **2024**, *24*, 34–46. https://doi.org/10.1109/MCAS.2024.3383808.
30. Anders, J.; Babaie, M.; Bardin, J.C.; Bashir, I.; Billiot, G.; Blokina, E.; Bonen, S.; Charbon, E.; Chiaverini, J.; Chuang, I.L.; et al. CMOS Integrated Circuits for the Quantum Information Sciences. *IEEE Trans. Quantum Eng.* **2023**, *4*, 5100230. https://doi.org/10.1109/TQE.2023.3290593.
31. Kang, K.; Minn, D.; Bae, S.; Lee, J.; Kang, S.; Lee, M.; Song, H.J.; Sim, J.Y. 40-nm Cryo-CMOS Quantum Controller IC for Superconducting Qubit. *IEEE J. Solid-State Circuits* **2022**, *57*, 3274–3287. https://doi.org/10.1109/JSSC.2022.3198663.
32. Charbon, E. Cryo-CMOS Electronics for Quantum Computing. *IEEE Solid-State Circuits Mag.* **2021**, *13*, 54–68. https://doi.org/10.1109/mssc.2021.3072808.
33. Craninckx, J.; Potocnik, A.; Parvais, B.; Grill, A.; Narasimhamoorthy, S.; Van Winckel, S.; Brebels, S.; Mongillo, M.; Li, R.; Govoreanu, B.; et al. CMOS Cryo-Electronics for Quantum Computing. In Proceedings of the IEEE International Electron Devices Meeting (IEDM), San Francisco, CA, USA, 12–18 December 2020; pp. 25.1.1–25.1.4. https://doi.org/10.1109/IEDM13553.2020.9371897.
34. Mehrpoo, M.; Patra, N.; Gong, J.; van Dijk, J.P.G.; Homulle, H.; Kiene, G.; Vladimirescu, A.; Sebastiano, F.; Charbon, E.; Babaie, M. Benefits and Challenges of Designing Cryogenic CMOS RF Circuits for Quantum Computers. In Proceedings of the IEEE International Symposium on Circuits and Systems (ISCAS), Sapporo, Japan, 26–29 May 2019; pp. 1–4. https://doi.org/10.1109/ISCAS.2019.8702452.
35. Patra, B.; Incandela, R.M.; van Dijk, J.P.G.; Homulle, H.A.R.; Song, L.; Shahmohammadi, M.; Staszewski, R.B.; Vladimirescu, A.; Babaie, M.; Sebastiano, F.; Charbon, E. Cryo-CMOS Circuits and Systems for Quantum Computing Applications. *IEEE J. Solid-State Circuits* **2018**, *53*, 309–321. https://doi.org/10.1109/JSSC.2017.2737549.
36. Sebastiano, F.; Homulle, H.; Patra, B.; Incandela, R.; van Dijk, J.; Song, L.; Babaie, M.; Vladimirescu, A.; Charbon, E. Cryo-CMOS Electronic Control for Scalable Quantum Computing. In Proceedings of the ACM/EDAC/IEEE Design Automation Conference (DAC), Austin, TX, USA, 18–22 June 2017; pp. 1–6. https://doi.org/10.1145/3061639.3072948.
37. Charbon, E.; Sebastiano, F.; Vladimirescu, A.; Homulle, H.; Visser, S.; Song, L.; Incandela, R.M. Cryo-CMOS for quantum computing. In Proceedings of the IEEE International Electron Devices Meeting (IEDM), San Francisco, CA, USA, 3–7 December 2016; pp. 13.5.1–13.5.4. https://doi.org/10.1109/IEDM.2016.7838410.

38. Severino, R.R.; Spasaro, M.; Zito, D. Silicon Spin Qubit Control and Readout Circuits in 22 nm FDSOI CMOS. In Proceedings of the IEEE International Symposium on Circuits and Systems (ISCAS), Virtual, 10–21 October 2020. https://doi.org/10.1109/ISCAS45731.2020.9180790.
39. Park, J.; Subramanian, S.; Lampert, L.; Mladenov, T.; Klotchkov I.; Kurian, D.J.; Juarez-Hernandez, E.; Esparza, B.P.; Kale, S.R.; Asma Beevi, K.T.; et al. A Fully Integrated Cryo-CMOS SoC for State Manipulation, Readout, and High-Speed Gate Pulsing of Spin Qubits. *IEEE J. Solid-State Circuits* **2021**, *56*, 3289–3306. https://doi.org/10.1109/JSSC.2021.3115988.
40. Yoo, J.; Chen, Z.; Arute, F.; Montazeri, S.; Szalay, M.; Erickson, C.; Jeffrey, E.; Fatemi, R.; Giustina, M.; Ansmann, M.; et al. Design and Characterization of a $\leq$ 4-mW/Qubit 28-nm Cryo-CMOS Integrated Circuit for Full Control of a Superconducting Quantum Processor Unit Cell. *IEEE J. Solid-State Circuits* **2023**, *58*, 3044–3059. https://doi.org/10.1109/JSSC.2023.3309317.
41. Silva, J.T.B.; Brito-Filho, F.A. Design and Cryogenic Evaluation of a 130 nm Cryo-CMOS Up-converter for Quantum Computing Applications. In Proceedings of the SBMO/IEEE MTT-S International Microwave and Optoelectronics Conference (IMOC), Campina Grande, Brazil, 9–12 November 2025; pp. 768–772. https://doi.org/10.1109/IMOC65414.2025.11365758.
42. Toth, P.; Eugine, P.S.; Kudabay, Y.; Yamashita, K.; Halama, S.; Parvizinejad, J.; Bonkowski, M.; Ishikuro, H.; Ospelkaus, C.; Issakov, V. A Cryo-BiCMOS Controller for Quantum Computers based on Trapped Beryllium Ions. *IEEE J. Solid-State Circuits* **2026**, *61*, 673–689. https://doi.org/10.1109/JSSC.2025.3632204.
43. Kwende, R.C.; Rosenstock, D.; Wang, C.; Bardin, J.C. A 6 mW Cryogenic SiGe Receiver IC For High-Fidelity Qubit Readout. In Proceedings of the IEEE/MTT-S International Microwave Symposium, Washington, DC, USA, 16–21 June 2024; pp. 874–877. https://doi.org/10.1109/IMS40175.2024.10600326.
44. Mani, H.; Mauskopf, P. A single-stage cryogenic LNA with low power consumption using a commercial SiGe HBT. In Proceedings of the 11th International Workshop on Low Temperature Electronics (WOLTE), Grenoble, France, 7–9 July 2014; pp. 17–20. https://doi.org/10.1109/WOLTE.2014.6881015.
45. Curry, M.J.; England, T.D.; Bishop, N.C.; Ten-Eyck, G.; Wendt, J.R.; Pluym, T.; Lilly, M.P.; Carr, S.M.; Carroll, M.S. Cryogenic preamplification of a single-electron-transistor using a silicon-germanium heterojunction-bipolar-transistor. *Appl. Phys. Lett.* **2015**, *106*, 203505. https://doi.org/10.1063/1.4921308.
46. Wong, W.T.; Coskun, A.H.; Bardin, J.C. Design and characterization of a wideband high-dynamic range SiGe cryogenic low noise amplifier. In Proceedings of the IEEE MTT-S International Microwave Symposium (IMS), Honolulu, HI, USA, 4–9 June 2017; pp. 1972–1975. https://doi.org/10.1109/MWSYM.2017.8059051.
47. Song, I.; Cardoso, A.S.; Ying, H.; Cho, M.K.; Cressler, J.D. Cryogenic Characterization of RF Low-Noise Amplifiers Utilizing Inverse-Mode SiGe HBTs for Extreme Environment Applications. *IEEE Trans. Device Mater. Reliab.* **2018**, *18*, 613–619. https://doi.org/10.1109/TDMR.2018.2878471.
48. Ying, H.; Rao, S.G.; Teng, J.W.; Frounchi, M.; Muller, M.; Jin, X.; Schroter, M.; Cressler, J.D. Compact Modeling of SiGe HBTs for Design of Cryogenic Control and Readout Circuits for Quantum Computing. In Proceedings of the IEEE BiCMOS and Compound Semiconductor IC and Technology Symposium (BCICTS), Online, 16–19 November 2020; pp. 1–4. https://doi.org/10.1109/BCICTS48439.2020.9392937.
49. Zou, Z.; Hosseini, M.; Kwende, R.; Raman, S.; Bardin, J.C. A frequency and bandwidth reconfigurable 3–6 GHz cryogenic SiGe BiCMOS LNA with a power consumption of $\leq$2.9 mW. In Proceedings of the IEEE MTT-S International Microwave Symposium (IMS), Atlanta, GA, USA, 6–11 June 2021; pp. 653–656. https://doi.org/10.1109/IMS19712.2021.9574918.
50. Hosseini, M.; Bardin, J.C. A 1 mW 0.1–3 GHz cryogenic SiGe LNA with an average noise temperature of 4.6K. In Proceedings of the IEEE MTT-S International Microwave Symposium (IMS), Atlanta, GA, USA, 6–11 June 2021; pp. 896–899. https://doi.org/10.1109/IMS19712.2021.9574993.
51. Bhaumik, S.; bij de Vaate, J.G. Hybrid LNAs with SiGe HBTs on 7th generation BiCMOS process. In Proceedings of the 44th European Microwave Conference, Rome, Italy, 5–10 October 2014; pp. 1388–1391. https://doi.org/10.1109/EuMIC.2014.6997888.
52. Peng, Y.; Ruffino, A.; Benserhir, J.; Charbon, E. A Cryogenic SiGe BiCMOS Hybrid Class B/C Mode-Switching VCO Achieving 201 dBc/Hz Figure-of-Merit and 4.2 GHz Frequency Tuning Range. In Proceedings of the IEEE International Solid-State Circuits Conference (ISSCC), San Francisco, CA, USA, 20–26 February 2022; Volume 65, pp. 364–366. https://doi.org/10.1109/ISSCC42614.2022.9731542.
53. Wu, R.; Wang, C. A 2–12 GHz SiGe BiCMOS Cryogenic LNA with 6K Noise Temperature and 1.3 mW DC Power. In Proceedings of the IEEE MTT-S International Microwave Workshop Series on Advanced Materials and Processes for RF and THz Applications (IMWS-AMP), Chengdu, China, 13–15 November 2023; pp. 1–3. https://doi.org/10.1109/IMWS-AMP57814.2023.10381379.
54. Lotfi, H.; Anders, J. Design of Compact Current-Drive Power Amplifiers for the Efficient Control of Spin Qubits. In Proceedings of the IEEE International Conference on Electronics, Circuits and Systems (ICECS), Istanbul, Turkey, 4–7 December 2023; pp. 1–4. https://doi.org/10.1109/ICECS58634.2023.10382801.
55. Peng, Y.; Benserhir, J.;Castaneda, M.; Fognini, A.; Bruschini, C.; Charbon, E. A 0.32 × 0.12 mm² cryogenic BiCMOS 0.1–8.8 GHz low noise amplifier achieving 4 K noise temperature for SNWD readout. *IEEE Trans. Microw. Theory Tech.* **2024**, *72*, 2179–2192. https://doi.org/10.1109/TMTT.2024.3354828.

56. Ton, B.; Prele, D.; Gonzalez, M.; Mesquida, J.; Charrier, D.; Chen, S. Cryogenic concept of a Low-Noise Amplifier using IHP130 nm BiCMOS technology. *IEEE Trans. Appl. Supercond.* **2026**, *36*, 2502407. https://doi.org/10.1109/TASC.2026.3681410.
57. Cressler, J.D.; Niu, G. *Silicon-Germanium Heterojunction Bipolar Transistors*; Hartech House: Vester Skerninge, Denmark, 2003; ISBN 978-1630812942.
58. Rucker, H.; Korn, J.; Schmidt, J. Operation of SiGe HBT at cryogenic temperatures. In Proceedings of the IEEE Bipolar/BiCMOS Circuits and Technology Meeting (BCTM), Miami, FL, USA, 19–21 October 2017; pp. 17–20. https://doi.org/10.1109/BCTM.2017.8112902.
59. Guo, Y.; Li, Y.; Huang, W.; Tian, T.; Wu, N.; Zhang, S.; Liu, Q.; Li, T.; Wang, Z.; Deng, N.; et al. A Cryogenic Superconducting Quantum Computing Unit Interface Chipset With Phase-Detection-Based Readout and Phase-Shifter-Based Controller. *IEEE J. Solid-State Circuits* **2026**, *61*, 5204–5221. https://doi.org/10.1109/JSSC.2026.3695612.
60. Van Dijk, J.P.G.; Patra, B.; Subramanian, S.; Xue, X.; Samkharadze, N.; Corna, A.; Jeon, C.; Sheikh, F.; Juarez-Hernandez, E.; Esparza, B.P.; et al. A Scalable Cryo-CMOS Controller for the Wideband Frequency-Multiplexed Control of Spin Qubits and Transmons. *IEEE J. Solid-State Circuits* **2020**, *55*, 2930–2946. https://doi.org/10.1109/JSSC.2020.3024678.
61. Chakraborty, S.; Kossel, M.; Brandli, M.; Francese, P.-A.; John, M.P.; Bulzacchelli, J.F.; Rosno, O.; Yeck, M.; Frolov, D.; Frank, D.J.; et al. Cryogenic CMOS RF AWGs for Qubit Control. *IEEE J. Solid-State Circuits* **2026**, *61*, 77–92. https://doi.org/10.1109/JSSC.2026.3660196.
62. Leung, B. *VLSI for Wireless Communication*; Springer: Berlin/Heidelberg, Germany, 2011; ISBN 978-1489973771.
63. Petrov, V.A. Bethe's Ansatz for Coulomb -Nuclear Interference Is Incompatible with Additive Eikonal. *arXiv* **2019**, arXiv:1906.03895.
64. Bardin, J.C.; Slichter, D.H.; Reilly, D.J. Microwaves in Quantum Computing. *IEEE J. Microw.* **2021**, *1*, 403–427. https://doi.org/10.1109/JMW.2020.3034071.
65. Bardin, J.C. Silicon Germanium Heterojunction Bipolar Transistors for Extremely Low-Noise Applications. Ph.D. Dissertation, California Institute of Technology, Pasadena, CA, USA, 2009.
66. Badiali, A.; Borgarino, M. Cryo-CMOS Multi-Frequency Modulator for 2-Qubit Controller. *Electronics* **2024**, *13*, 2546. https://doi.org/10.3390/electronics13132546.
67. Kossel, M.; Brändli, M.; Prathapan, M.; Morf, T.; Francese, P.A.; Zota, C.; Ruffino, A.; Almagro, P.S.; Oropallo, M.V.; Heim, D.; et al. A 40 GS/s 8b-DAC SST-TX in 7 nm FinFET CMOS for cryogenic quantum applications with 32 kB SRAMbased RF-DDS AWG. In Proceedings of the 2024 IEEE European Solid-State Electronics Research Conference (ESSERC), Bruges, Belgium, 9–12 September 2024; pp. 161–164. https://doi.org/10.1109/ESSERC62670.2024.10719419.
68. Girard, A. *Invention Nouvelle en l'Algebre*; Guillaume Iansson Blaeuw: Amsterdam, The Netherlands, 1629.
69. Cardano, G. *Artis Magnae Sive De Regulis Algebraicis*; Johannes Petreius: Nuremberg, Germany, 1545.

Disclaimer/Publisher's Note: The statements, opinions and data contained in all publications are solely those of the individual author(s) and contributor(s) and not of MDPI and/or the editor(s). MDPI and/or the editor(s) disclaim responsibility for any injury to people or property resulting from any ideas, methods, instructions or products referred to in the content.